Diagnosis of spatiotemporal chaos in wave envelopes of a nematic electroconvection pattern

G. Dangelmayr,[1] G. Acharya,[2] J. T. Gleeson,[2] I. Oprea,[1] and J. Ladd[1]

[1]*Department of Mathematics, Colorado State University, Fort Collins, Colorado 80523, USA*
[2]*Department of Physics, Kent State University, Kent, Ohio 44242, USA*

In this paper we report and analyze complex spatiotemporal dynamics recorded in electroconvection in the nematic liquid crystal I52, driven by an ac voltage slightly above the onset value. The instability mechanism creating the pattern is an oscillatory (Hopf) instability, giving rise to two pairs of counterpropagating rolls traveling in oblique directions relative to the unperturbed director axis. If a system of nonlinear partial differential equations shows the same set of unstable modes, the pattern above the onset is represented in a weakly nonlinear analysis as a superposition of the traveling rolls in terms of wave envelopes varying slowly in space and time. Motivated by this procedure, we extract slowly varying envelopes from the space-time data of the pattern, using a four-wave demodulation based on Fourier analysis. In order to characterize the spatiotemporal dynamics, we apply a variety of diagnostic methods to the envelopes, including the calculation of mean intensities and correlation lengths, global and local Karhunen-Loève decompositions in Fourier space and physical space, the location of holes, the identification of coherent vertical structures, and estimates of Lyapunov exponents. The results of this analysis provide strong evidence that our pattern exhibits extensive spatiotemporal chaos. One of its main characteristics is the presence of coherent structures of low and high intensities extended in the vertical (parallel to the director) direction.

I. INTRODUCTION

Spatially extended systems driven far from equilibrium may exhibit complex spatiotemporal patterns, characterized by a fast decay of spatial and temporal correlations [1]. Such states are referred to as spatiotemporal chaos (STC). Owing to the coupling of many spatial degrees of freedom, STC often shows structures richer than the purely temporally chaotic states observed in low-dimensional systems. In particular, extensive STC is a state in which several dynamical invariants used for the characterization of low-dimensional chaos, such as the fractal dimension and the number of positive Lyapunov exponents, scale with the system's volume and become extensive variables. The problem of finding a general framework for the characterization of such disordered states, as well as the identification of instability mechanisms generating them, is still an open question in nonlinear dynamics. While spatiotemporally chaotic phenomena have received a great deal of attention in the last decade, much of this work is theoretical and numerical, calling for a more systematic analysis of experiments. In this paper we report and study a complex spatiotemporal pattern recorded in an electroconvection experiment with the nematic liquid crystal I52, which exhibits the characteristics of extensive STC.

Many theoretical investigations of STC focused on the one-dimensional (1D) and two-dimensional (2D) complex Ginzburg-Landau equations, which are known to exhibit phase turbulence and defect chaos; see [2] for a review. The importance of this, and more generally systems of coupled Ginzburg-Landau equations, relies on the fact that these equations occur in a weakly nonlinear analysis of nonlinear systems of partial differential equations (PDEs) slightly above the primary instability of a basic, homogeneous state. Their solutions describe the dynamics of slowly varying en-

velopes of plane-wave trains associated with the critical wave numbers. Thus, in order to relate an experimentally observed spatiotemporally chaotic pattern to the solutions of a system of Ginzburg-Landau equations, the STC has to arise directly above the onset. This excludes, for example, the spiral defect chaos observed in Rayleigh-Bénard convection [3,4], a prototype of STC, because it emerges from an already complicated state. A further complication is that the equations for Rayleigh-Bénard convection in 2D extended fluid layers are isotropic, which leads to a full circle of critical wave numbers that makes the description through a finite set of plane-wave envelopes problematic. In contrast, in anisotropic systems there is only a finite, usually small number of critical wave numbers, which allows a unique reduced description through a finite set of plane-wave envelopes above the onset, whose dynamics is governed by Ginzburg-Landau-type amplitude equations.

A paradigm for anisotropic pattern formation is the electroconvection in nematic liquid crystals [5–7]. Due to the short characteristic time scales and large aspect ratios, nematic electroconvection is a well-suited experimental system in which to study ordered and complex spatiotemporal patterns, by varying the electrical conductivity and the amplitude and frequency of the electric potential difference across a planar layer of the liquid crystal. The anisotropy results from an inherent order of the molecules relative to each other. The direction parallel to the local average molecular alignment is referred to as director. The plates are treated so that there is a uniform alignment of the director parallel to the plates, i.e., planar alignment, which induces an axial anisotropy.

Nematic electroconvection has been intensively studied experimentally. Depending upon the control parameters and the material used, a great variety of patterns, including stationary and traveling rolls, localized patterns, spatiotemporal chaos, and rectangular patterns [8–14] have been observed at

or near onset. Most of the phenomena observed near threshold (e.g., normal, oblique, and dielectric rolls and the structure and dynamics of defects) can be understood from the "standard" hydrodynamic description, which combines the continuum theory of Ericksen and Leslie with the quasistatic Maxwell equations. Notable exceptions are the experimentally observed oscillatory instabilities [11,15] leading to traveling rolls. The recently introduced and analyzed weak electrolyte model [13,16] explains these effects as a consequence of a slow dissociation and recombination of the charge-carrying ions, resulting in a dynamically varying electric conductivity. If the relaxation of the conductivity is sufficiently slow, the competition between stabilizing and destabilizing effects leads to an oscillatory convective instability with a nonzero Hopf frequency [13,17–19], giving rise to convection rolls traveling in the director direction, or in oblique directions relative to the director. We refer to the latter case as "oblique Hopf instability."

In a series of papers, Dennin *et al.* [10,11,15] reported a variety of ordered and complex patterns observed in electroconvection in the nematic liquid crystal I52. The complex patterns include localized worm structures, as well as two types of patterns identified as STC. One of these two states occurs directly at the onset, when the convective instability is an oblique Hopf instability. The state arises as a superposition of two pairs of counterpropagating traveling rolls created in the instability. One of its main characteristics is that it is extended over the entire convection cell, but as yet there is no complete investigation confirming that it is extensive STC.

In this paper we report and analyze a complex electroconvection pattern that is characterized by the appearance of vertical active (high-intensity) regions in the cell, separated by inactive (low-intensity) regions. Like the fully extended STC state reported in [11,15], it is observed slightly above the onset and arises as a superposition of four oblique traveling rolls created in the oblique Hopf instability. Our main objective is to extract slowly varying envelopes of these waves through a spatiotemporal demodulation analysis, and to study their dynamics using a variety of numerical diagnostic tools. This approach to analyzing the pattern is guided by the procedure of a weakly nonlinear analysis of a governing system of partial differential equations, such as the weak electrolyte model [18–20]. Although in this paper we do not actually pursue a weakly nonlinear analysis of the weak electrolyte model, which determines the parameters in the Ginzburg-Landau equations for the envelopes, our study bridges the gap between experimentally observed STC and the dynamics of envelopes. Work toward identifying the parameters in the weak electrolyte model for this and other experiments, and calculating the resulting Ginzburg-Landau parameters is in progress.

The paper is organized as follows. In Sec. II we briefly describe the oblique Hopf instability and the representation of patterns through slowly varying envelopes. In Sec. III we discuss the experimental setup, and in Sec. IV the demodulation analysis for extracting the envelopes. Section V is devoted to the analysis of the spatiotemporal dynamics of the envelopes using a variety of diagnostic tools. These include the calculation of mean intensities, global and local

Karhunen-Loève decompositions (KLDs), the location of holes, the identification of coherent vertical structures, estimates of Lyapunov exponents, a space-time cluster analysis, and the identification of ideal wave patterns characteristic of the oblique Hopf instability. The results of this study suggest that the recorded pattern is a case of extensive STC that exhibits spatiotemporal intermittency. Section VI concludes with discussions and an outlook on future work.

II. OBLIQUE HOPF INSTABILITY

In this section we briefly describe the oblique Hopf instability in 2D extended layers, and the representation of solutions through slowly varying envelopes as prescribed in a weakly nonlinear analysis.

If an axially anisotropic system of PDEs undergoes the oblique Hopf instability, there are four critical wave numbers $(\pm p_c, \pm q_c)$ located off both reflection axes. A scalar field u on, say, the top of the layer is represented in the form

$$u(x,y,t) \sim (A_1 W_1 + A_2 W_2 + A_3 W_3 + A_4 W_4 + \text{c.c.}) + \text{hot},$$

(1)

where the $A_j = A_j(x,y,t)$, with $j = 1, \ldots, 4$, are slowly varying complex envelopes modulating four oblique traveling waves,

$$W_1 = e^{i(p_c x + q_c y + \omega_c t)}, \quad W_2 = e^{i(-p_c x + q_c y + \omega_c t)},$$

$$W_3 = e^{i(-p_c x - q_c y + \omega_c t)}, \quad W_4 = e^{i(p_c x - q_c y + \omega_c t)},$$

(2)

ω_c is the critical frequency, and the waves W_j in Eq. (2) arise in the solutions of the linearized system at onset. For the weak electrolyte model, x is the coordinate along the director direction, and y is the coordinate in the perpendicular direction. In Eq. (1), c.c. refers to the complex-conjugate expression, and hot to higher harmonics. Formally, in an expansion in terms of a small parameter ε measuring the distance of the control parameter (voltage in the case of the weak electrolyte model) from the onset value, the A_j are of order $O(\sqrt{\varepsilon})$. At $O(\varepsilon)$ the hot comprise terms of the form $A_i A_j W_i W_j$, $A_i \bar{A}_j W_i \bar{W}_j$ (the bars denote complex conjugation) and their complex conjugates, and similarly at higher orders. Thus the envelopes of the higher harmonics are "slaved" by the basic envelopes A_j. The A_j in turn satisfy a system of coupled Ginzburg-Landau equations [21,22], and so are the main driver of the dynamics.

The waves W_2 and W_4 are stripes propagating in the directions $\pm(-p_c, q_c)$ and are referred to as "zig waves," whereas W_1 and W_3 propagate in the directions $\pm(p_c, q_c)$ and are referred to as "zag waves." Accordingly, A_2, A_4 and A_1, A_3 are referred to as zig and zag envelopes, respectively. The zig and zag waves are pairs of counterpropagating traveling waves moving "left" (W_1, W_4) and "right" (W_2, W_3), as illustrated in Fig. 1.

The envelopes $A_1, \ldots, A_4$ satisfy a system of coupled Ginzburg-Landau equations derived in a weakly nonlinear analysis. The form of these equations follows from symmetry considerations and the type of the instability [21,22]. They show a rich variety of solutions, which is only partly explored [19,20,22]. There are six distinguished spatially ho-
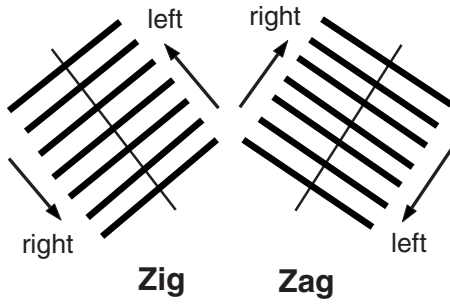
FIG. 1. Illustration of zig and zag waves moving left or right.

mogeneous solutions corresponding to traveling waves, standing waves, two types of traveling rectangles (TRs), standing rectangles (SRs), and alternating waves (AWs) [23,24]. The main characteristics of the STC pattern reported in [9,11,15] are extended patches of alternating waves. In our pattern ideal waves are observed only in small patches and over short time ranges, and the dominant waves are zag waves and traveling rectangles.

In this paper, instead of simulating the Ginzburg-Landau equations for the A_j, we extract the envelopes from the experimentally recorded pattern using Fourier analysis.

III. EXPERIMENTAL SETUP

In the past 40 years, electroconvection experiments have employed a variety of different nematic liquid-crystal compounds and mixtures, including Phase V, a mixture of azoxy compounds [8,13,25–27]; Mischung V, a mixture of phenyl benzoates [28–32]; and methoxybenzylidene butylaniline (MBBA), a single component [33–35]. MBBA is one of the earliest thermotropic nematic liquid crystals, and has the advantage that practically all of its physical properties have been measured. Even though it has suitable values of dielectric anisotropy (ϵ_a) and conductivity anisotropy (σ_a) in order for electroconvection to occur, its chemical stability is problematic. Also, ϵ_a is roughly -0.5 (depending on temperature), which is low if one desires oblique ("zig-zag") modes [9,36] with a relatively large angle between the director and the wave vector. We have therefore utilized a single component nematic liquid crystal, 4-ethyl-2-fluoro-4′-[2-(*trans*-4-pentylcyclohexyl)-ethyl]biphenyl [9,37], usually referred to by its trade name, I52. It has a wide nematic range from 24 to 103.4 °C, is chemically stable, and has ϵ_a low enough so as to exhibit distinct oblique traveling rolls, with greater oblique angles at low frequencies when adequately doped [9,11]. Also, I52 reliably exhibits a supercritical Hopf bifurcation at onset [14], giving rise to left- and right-traveling zig and zag rolls (oblique Hopf instability), whose dynamics slightly above onset is governed by four coupled Ginzburg-Landau equations [21,22].

We used the traditional electroconvection arrangement, in which a ready-made cell fabricated by E.H.C. Co., Tokyo, Japan (EHC-cell) with flat, transparent conducting electrodes is rubbed to get planar alignment along a single direction. In the parallel-plate-capacitor geometry, the electrodes were separated by a distance of 10.39 ± 0.08 μm (measured inter-

ferometrically), and the lateral dimensional "active area" was 10×10 mm^2. Outside the active area, there is no conductive coating and hence no electric field is present. The electrical contact between the plates and the hookup wires were made by using silver-laden epoxy.

One challenge with I52 is preparing the material so that it has the electrical conductivity required for the desired electroconvection state. The most reliable dopant for increasing I52's conductivity is reported to be molecular iodine, I$_2$. However, achieving the desired conductivity requires more than simply adding iodine to the nematic liquid crystal, because the dopant is not highly soluble. Our approach was to hasten the dissolution by holding the mixture at elevated temperature (150 °C for 72 h). Although temperature this high can subtly affect the liquid crystal's material properties, particularly the dielectric anisotropy, we confirmed that this change was not only small, but also reproducible. Thus, material prepared in this way was found to give reliable and repeatable results for not only the electrical conductivity, but also the electroconvection behavior.

For the experiment reported here, the nominal concentration of iodine was fairly high: 11 wt %. On face of it, this is a large quantity of dopant, but we have observed, as have other researchers [12,38], that what is critical is not the nominal concentration, but its effect on the electrical conductivity and the resulting electroconvective threshold curve; these results are presented subsequently. One further issue well known with I52 is the control of electrical conductivity during experiments [9], since this changes over time elapsed. To maintain a constant value of the conductivity throughout the experiment, one typically adjusts the temperature within the range where $\epsilon_a < 0$. In our case, ϵ_a became positive at 62.95 °C.

In order to obtain both $\epsilon_\perp$ and $\sigma_\perp$ at different frequencies, we measured the current passing through the liquid-crystal cell at a constant voltage. The result is the sum of conduction current and the displacement current [39]. Thus, for no convection, the current J can be expressed as

$$J = \sqrt{2}V(G_\perp \cos \omega_o t - \omega_o C_\perp \sin \omega_o t), \qquad (3)$$

where V is the signal voltage, and $G_\perp$ and $C_\perp$ are the perpendicular components of the conductance and capacitance, respectively. We can calculate $\sigma_\perp$ from the in-phase part of Eq. (3) and $\epsilon_\perp$ from the out-of-phase part. For this experiment, the sequence of images recorded had $\epsilon_\perp = 2.88$ and $\sigma_\perp = 11.37 \times 10^{-9}$ Ω^{-1} m^{-1} at 51 Hz, and the thickness of the cell was 10.39 μm.

The electroconvection apparatus consists of a temperature-controlled stage, which besides controlling the temperature can precisely control heating as well as cooling, electronics for applying the ac voltage, and the shadowgraph apparatus [40] for visualization. The cell was illuminated by polarized light with the polarization along the director, and the resulting shadowgraph images were monitored by the charge-coupled device (CCD) camera mounted on the microscope at 30 cm from the sample, using a $10\times$ objective. Besides other advantages, the small thickness of the cell and the lower magnification of the microscope enabled us to capture more rolls in the individual frames.

We fixed the temperature to 30 °C and the external driving frequency to 51 Hz in the conduction regime (the cutoff frequency at this temperature was 340 Hz), and slowly increased the ac voltage V to the onset voltage V_c. After V_c was reached, we slightly increased the voltage further $[\varepsilon = (V/V_c)^2 - 1 \approx 0.042]$, waited for a few minutes, and then captured the 8-bit grayscale image and calculated its power spectrum in real time. This allowed finer focusing of the shadowgraph in order to enhance the dominant inner oblique modes (first harmonics) of the power spectrum right above onset. With improper focusing, the higher harmonics dominate over the first harmonics. The sample stage, kept on the fully rotatable stage of the microscope, was rotated as necessary to make sure that the peaks of the power spectrum were symmetric about the director axis. Then the stage was fixed for the whole experiment, and we captured a sequence of images using a frame grabber at the rate of 28.53 frames/s.

The raw data recorded in this experiment consist of a sequence of $T = 30\,000$ digital images of size $M \times N$, with (using matrix notation) $M = 480$ pixels in the vertical (the director) direction and $N = 640$ pixels in the horizontal direction. In order to remove inhomogeneities in the optical system, the raw images have been preprocessed pixelwise according to the equation

$$I = \frac{\langle F_f - F_d \rangle_p}{F_f - F_d}(I_r - F_d),$$

where I is the preprocessed (flatfielded) image; I_r is the raw image; F_d is the dark frame (no light input); F_f is the flat field, which is a map of the CCD's sensitivity to light at zero ac field and same illumination and temperature as the raw image; and $\langle F_f - F_d \rangle_p$ denotes the average of $F_f - F_d$ over all pixels.

IV. FOUR-WAVE DEMODULATION

Since the applied voltage is slightly above the critical value for the onset of electroconvection, created in an oblique Hopf instability, our objective is to extract envelopes varying slowly in space and time as prescribed in a weakly nonlinear analysis of a system of PDEs. This analysis also yields the values of the critical wave numbers and the critical (Hopf) frequency. The dynamics of the envelopes is studied in Sec. V.

We first perform a spatial demodulation that generates amplitudes of zig and zag waves varying slowly in space, but not yet in time, following the procedure used in [9,11,15]. In the second step we perform a temporal demodulation, in which we extract the envelopes of the four oblique traveling waves from the time series of the zig and zag amplitudes. This separation into spatial and temporal demodulation bypasses full three-dimensional (3D) Fourier transforms, which significantly reduces the computational effort.

A. Spatial demodulation and critical wave numbers

We denote the sequence of flatfielded images by $I(k,l,t)$, where k and l are the vertical and horizontal pixel labels, $0 \le k < M$ and $0 \le l < N$, and t is time, $0 \le t < T$. A typical

snapshot, recorded at $t = 20\,009$, is shown in Fig. 2(a). The discrete Fourier transform of an image is denoted by $F(m,n,t) = \mathcal{F}_s[I](m,n,t)$, defined by

$$\mathcal{F}_s[I] \equiv \frac{1}{\sqrt{MN}} \sum_{k=0}^{M-1} \sum_{l=0}^{N-1} e^{-2\pi i(mk/M + nl/N)} I(k,l,t), \qquad (4)$$

and its (spatial) power spectrum by $P(m,n,t) = |F(m,n,t)|^2$, where $\mathcal{F}_s$ refers to the spatial Fourier operator. We identify wave numbers with the integer labels (m,n), and note that F and P are doubly periodic in (m,n) with periods (M,N). Given F, the image can be reconstructed via the inverse Fourier transform, $I(k,l,t) = \mathcal{F}_s^{-1}[F](k,l,t)$, defined by

$$\mathcal{F}_s^{-1}[F] \equiv \frac{1}{\sqrt{MN}} \sum_{m=0}^{M-1} \sum_{n=0}^{N-1} e^{2\pi i(mk/M + nl/N)} F(m,n,t). \qquad (5)$$

For displaying Fourier transforms and power spectra, we choose the range $-M/2 \le m < M/2$ and $-N/2 \le n < N/2$ as fundamental wave-number domain. Note that, since I is real, $F(-m,-n,t) = \bar{F}(m,n,t)$.

In Fig. 2(b) the power spectrum P of the image at $t = 20\,009$ is displayed in the window $-55 \le m \le 55$, $-65 \le n \le 65$. Outside of this window P is negligibly small. We can clearly recognize small regions with high contributions from the dominant zig and zag modes (inner, first harmonics). The relatively strong contributions centered around the second harmonics of these modes do not arise from the fluid flow, but rather are an optical-focusing effect caused by the nonlinearities of the shadowgraph method; see [11,40] for a detailed explanation. Lastly, visible in Fig. 2(b) is the remnant after flatfielding, described in Sec. III. This operation reduced the longest-wavelength Fourier components by 90% over the raw image; the contributions near the center (0,0) are what remained.

In Fig. 2(c) we show zooms into the zig and zag regions of Fig. 2(b) in the windows W_{zig} and W_{zag}, defined by $M_1 \le |m| \le M_2$, $N_1 \le n \le N_2$, with $m < 0$ for W_{zig} and $m > 0$ for W_{zag}. The cutoffs are chosen as $M_1 = 13$, $M_2 = 29$, $N_1 = 6$, and $N_2 = 39$; that is, the size of the windows is $M_w \times N_w$ with $M_w = 17$ and $N_w = 34$. We identify the modes in these windows (and their reflections about the origin) with the dominant oblique zig and zag modes, and denote the power spectra restricted to these windows by P_{zig} and P_{zag}.

The same zooms as in Figs. 2(b) and 2(c) are shown in Figs. 2(d) and 2(e) for the time-averaged power spectrum

$$\langle P \rangle(m,n) = \frac{1}{T} \sum_{t=0}^{T-1} P(m,n,t).$$

As for the snapshots, the restrictions of $\langle P \rangle$ to the windows W_{zig} and W_{zag} are identified with the averaged zig and zag power spectra and denoted $\langle P_{zig} \rangle$ and $\langle P_{zag} \rangle$. Their maxima are at $(m,n) = (-20, 22)$ and $(22,22)$. Note that the $\langle P_{zag} \rangle$ distribution is about three times as large as the $\langle P_{zig} \rangle$ distribution. Thus the pattern is on average dominated by the zag waves.
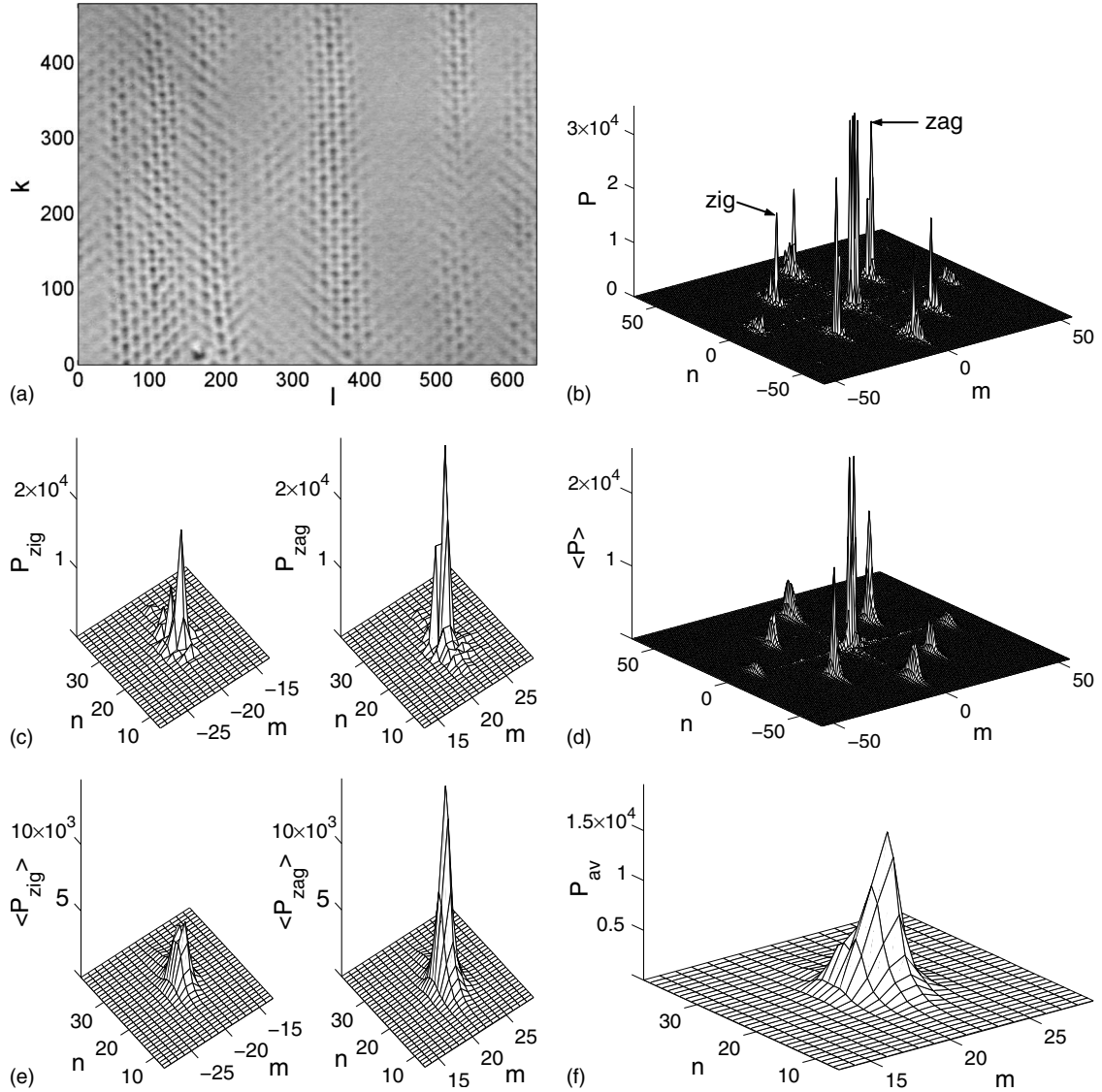
FIG. 2. (a) Flatfielded image at $t=20\,009$ and (b) its power spectrum in the window $-55 \leq m \leq 55$, $-65 \leq n \leq 65$. (c) Zooms of (b) into the oblique regions W_{zig} and W_{zag}. [(d) and (e)] Time-averaged (over the full range $0 \leq t < T$) power spectra in the same windows as in (b) and (c). (f) Time- and zig-zag-averaged power spectrum P_{av}. This distribution is used to compute the critical wave numbers (m_c, n_c) according to Eq. (7).

To each image we associate zig and zag components by filtering out the modes in the corresponding windows. This is done by setting $F_{zig} = \mathcal{M}_{zig}F$ and $F_{zag} = \mathcal{M}_{zag}F$, where $\mathcal{M}_{zig}$ and $\mathcal{M}_{zag}$ are filter masks which are zero outside of W_{zig} and W_{zag} and one inside these windows, except in a boundary layer of thickness of 4 pixels in which they decay to zero in order to avoid sharp discontinuities. The zig and zag components are then defined by

$$I_{zig} = \mathcal{F}_s^{-1}[F_{zig} + \hat{F}_{zig}], \quad I_{zag} = \mathcal{F}_s^{-1}[F_{zag} + \hat{F}_{zag}],$$

where $\hat{F}_{zig}(m,n,t) = \bar{F}_{zig}(-m,-n,t)$, and analogously $\hat{F}_{zag}$. In Figs. 3(a)–3(c) we show the components I_{zig} and I_{zag}, and their superposition $I_{zig} + I_{zag}$ at $t=20\,009$, respectively. In these and other grayscale (or online color-coded) plots, white is mapped to high values and black to low values.

To complete the spatial demodulation, we have to determine integer values (m_c, n_c) for the critical wave numbers. For this we use the time-averaged power spectra. We define, in the window W_{zag}, the zig-zag average $P_{av}(m,n)$ by

$$P_{av}(m,n) = \langle P_{zig} \rangle(-m,n) + \langle P_{zag} \rangle(m,n), \quad (6)$$

and interpret P_{av} as a (non-normalized) distribution for (m,n); see Fig. 2(f). The critical wave numbers are then defined as the averages with respect to this distribution,

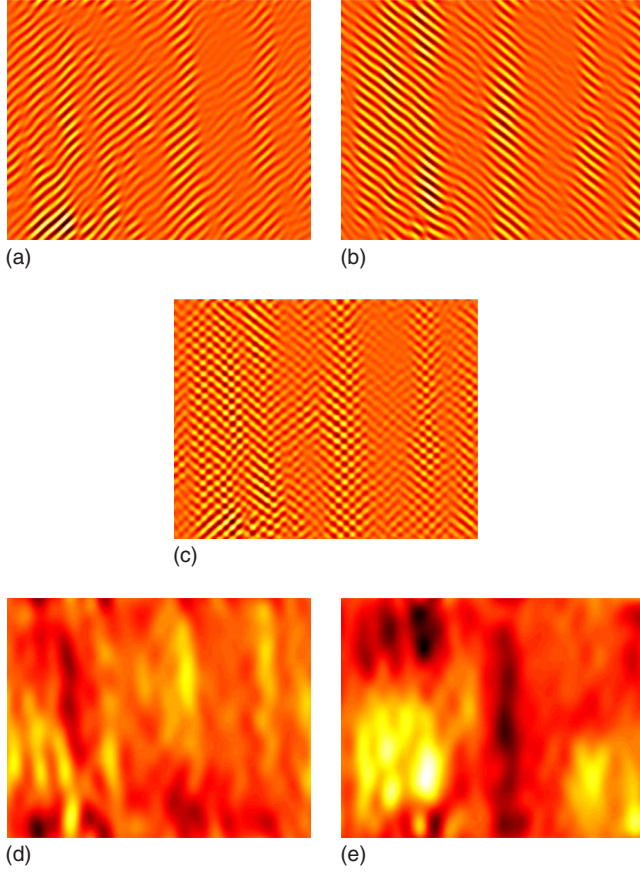$$(m_c, n_c) = \frac{1}{N_P} \sum_{m=M_1}^{M_2} \sum_{n=N_1}^{N_2} (m,n) P_{av}(m,n) = (21, 22), \quad (7)$$

where

FIG. 3. (Color online) (a) I_{zig}, (b) I_{zag}, (c) $I_{\text{zig}}+I_{\text{zag}}$, (d) A_{zig}, and (e) A_{zag} for the pattern snapshot at $t=20\,009$. Same grayscale (color online) maps for (a) and (b), and (d) and (e).

$$N_P = \sum_{m=M_1}^{M_2} \sum_{n=N_1}^{N_2} P_{\text{av}}(m,n).$$

The associated vertical and horizontal wavelengths are $(\lambda_v,\lambda_h)=(M/m_c,N/n_c)\times d_p$, where $d_p=0.746$ μm is the pixel diameter, yielding $\lambda_v=17.06$ μm and $\lambda_h=21.71$ μm.

Using the critical wave numbers, we can extract demodulated zig and zag envelopes $A_{\text{zig}}(k,l,t)$ and $A_{\text{zag}}(k,l,t)$ varying slowly in space (but not in time), by setting

$$A_{\text{zig}} = \mathcal{F}_s^{-1}[F_{\text{zig}}](k,l,t)e^{2\pi i(km_c/M-ln_c/N)} + \text{c.c.}, \quad (8)$$

$$A_{\text{zag}} = \mathcal{F}_s^{-1}[F_{\text{zag}}](k,l,t)e^{-2\pi i(km_c/M+ln_c/N)} + \text{c.c.} \quad (9)$$

In Figs. 3(d) and 3(e), A_{zig} and A_{zag} are displayed for $t=20\,009$. The dark and white (online yellow) regions in these plots are regions with high zig and high zag contributions to the recorded image.

B. Temporal demodulation and Hopf frequency

Due to the presence of a Hopf instability, the time series of the dominant oblique modes exhibit fast oscillations. The frequency range of these oscillations and the Hopf frequency are determined from the temporal power spectra of the oblique modes.

Given any time series $f(t)$, with $0\le t<T$, we denote by

$$g(w) = \mathcal{F}_t[f](w) \equiv \frac{1}{\sqrt{T}}\sum_{t=0}^{T-1} f(t)e^{-2\pi iwt/T} \quad (10)$$

its Fourier transform and by $s(w)=|g(w)|^2$ its power spectrum, where $\mathcal{F}_t$ refers to the temporal Fourier operator. In this discrete setting, temporal frequencies are identified with integers w in the range $-T/2\le w<T/2$.

The critical Hopf frequency is determined in a similar manner as the critical wave numbers. Here we use the averages of the temporal power spectra,

$$\langle S_{\text{zig/zag}}\rangle(w) = \frac{1}{M_w N_w}\sum |G_{\text{zig/zag}}(m,n,w)|^2,$$

where $G_{\text{zig/zag}}(m,n,w)=\mathcal{F}_t[F_{\text{zig/zag}}](m,n,w)$ and the sum extends over labels $(m,n)\in W_{\text{zig/zag}}$. These averages are displayed in Fig. 4(a) in the range of $|w|\le 2500$. Outside of this range $\langle S_{\text{zig}}\rangle$ and $\langle S_{\text{zag}}\rangle$ are very small, as are the spectra of the individual oblique modes' time series. As apparent from Fig. 4(a), the fast oscillations arise from contributions to the power spectra from left and right windows centered around $w\approx\pm 1500$. We choose these windows as $W_\pm$: $700\le|w|\le 2400$, with $w>0$ for W_+ and $w<0$ for W_-. In contrast to the spatial power spectra, the temporal power spectra do not exhibit strong contributions from the higher harmonics. Apart from the central peak at $w=0$, which results from a nonzero time average of the flatfielded images, the power spectra are dominated by contributions from the windows W_+ and W_-. Thus we use the zig-zag and left-right average

$$S_{\text{av}}(w) = \langle S_{\text{zig}}\rangle(w) + \langle S_{\text{zag}}\rangle(w) + \langle S_{\text{zig}}\rangle(-w) + \langle S_{\text{zag}}\rangle(-w)$$

[see Fig. 4(b)] as distribution to compute the (integer) Hopf frequency w_c in W_+ as

$$w_c = \sum_{w\in W_+} wS_{\text{av}}(w) \bigg/ \sum_{w\in W_+} S_{\text{av}}(w) = 1434.$$

With the camera's sampling rate of 28.53 frames/s, w_c corresponds to a frequency of 1.364 Hz.

We note that the distribution $s_{\text{av}}(w)$, which is derived from the power spectra of the critical modes $F(\pm m_c,n_c,t)$ in the same manner as $S_{\text{av}}(w)$ is derived from the averaged power spectra, gives an average of 1435. Thus the power spectra of the critical modes yield approximately the same critical frequency like the averaged power spectra.

Using w_c, we extract slow time series from the oblique modes by setting

$$F_{\text{zig/zag}}^\pm(m,n,t) = \mathcal{F}_t^{-1}[G_{\text{zig/zag}}^\pm](m,n,t)e^{-2\pi iw_c t/T}, \quad (11)$$

where

$$G_{\text{zig/zag}}^+(m,n,w) = \mathcal{M}(w)G_{\text{zig/zag}}(m,n,w),$$

$$G_{\text{zig/zag}}^-(m,n,w) = \mathcal{M}(w)\bar{G}_{\text{zig/zag}}(m,n,w),$$

and $\mathcal{M}(w)$ is a frequency filter mask which is 0 outside of W_+, 1 in the interior of W_+, and decays to 0 in transition regions of length 100 at the left and right boundaries of W_+.
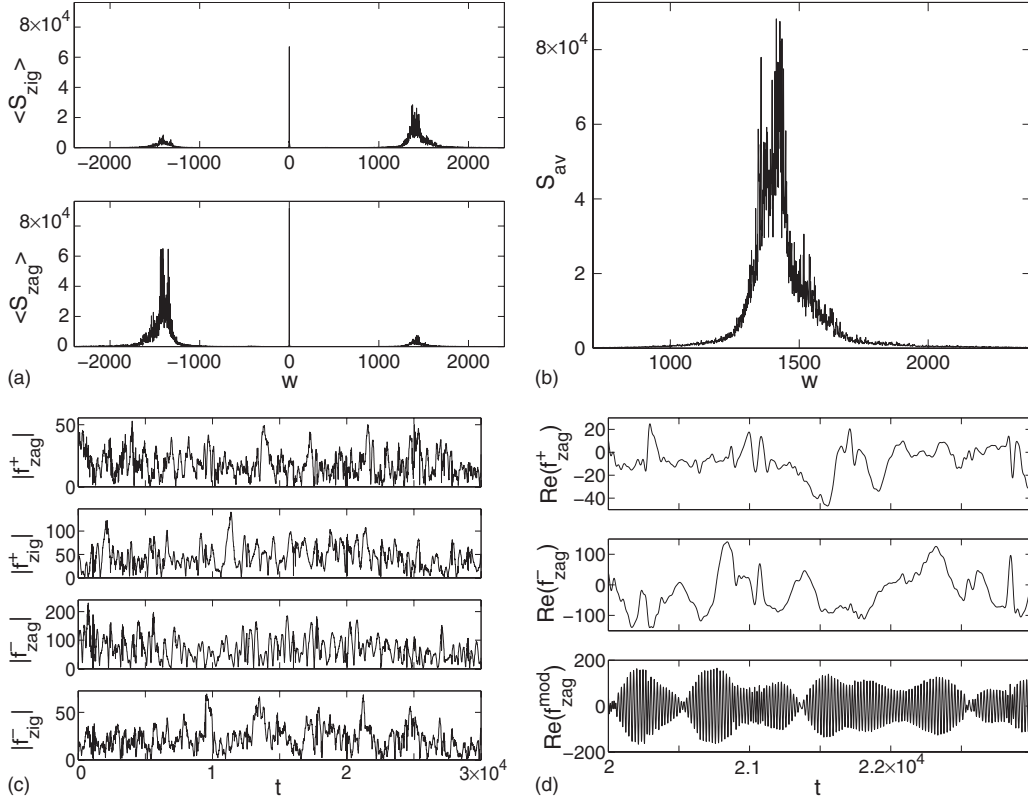
FIG. 4. (a) Averages $\langle S_{\text{zig/zag}} \rangle(w)$ over the temporal power spectra of all zig/zag modes. (b) Zig-zag and left-right average $S_{\text{av}}(w)$ of the averaged power spectra in (a). This distribution is used to compute w_c. (c) Moduli of the slow critical modes' time series $f_{\text{zig/zag}}^{\pm}(t)$, and (d) zooms of the real parts of $f_{\text{zag}}^{\pm}(t)$ and of the modulated time series $f_{\text{zag}}^{\text{mod}}(t)$ in the range $20\,000 \leq t \leq 23\,000$.

In Fig. 4(c) we show the moduli of the slow time series of the critical modes,

$$f_{\text{zig}}^{\pm}(t) = F_{\text{zig}}^{\pm}(m_c, n_c, t), \quad f_{\text{zag}}^{\pm}(t) = F_{\text{zag}}^{\pm}(-m_c, n_c, t), \quad (12)$$

over the full range $0 \leq t < T$. The fast oscillations seen in $f_{\text{zig}}(t)$ and $f_{\text{zag}}(t)$ have disappeared, and there is no discernible structure in phase plane as well as 3D plots of the slow modes. Zooms of the real parts of the slow critical zag modes in the window $20\,000 \leq t \leq 23\,000$, together with the real parts of the modulated time series,

$$f_{\text{zag}}^{\text{mod}}(t) = f_{\text{zag}}^{+}(t) e^{2\pi i w_c t/T} + \bar{f}_{\text{zag}}^{-}(t) e^{-2\pi i w_c t/T},$$

are shown in Fig. 4(d).

We finally define envelopes varying slowly in time and space through spatial Fourier inversion as

$$A_1(k,l,t) = \mathcal{F}_s^{-1}[F_{\text{zag}}^{+}](k,l,t) e^{2\pi i(-m_c k/M - n_c l/N)},$$

$$A_2(k,l,t) = \mathcal{F}_s^{-1}[F_{\text{zig}}^{+}](k,l,t) e^{2\pi i(m_c k/M - n_c l/N)},$$

$$A_3(k,l,t) = \mathcal{F}_s^{-1}[\widetilde{F}_{\text{zag}}^{-}](k,l,t) e^{2\pi i(m_c k/M + n_c l/N)},$$

$$A_4(k,l,t) = \mathcal{F}_s^{-1}[\widetilde{F}_{\text{zig}}^{-}](k,l,t) e^{2\pi i(-m_c k/M + n_c l/N)}, \quad (13)$$

where $\widetilde{F}_{\text{zig/zag}}^{-}(m,n,t) = F_{\text{zig/zag}}^{-}(-m,-n,t)$. The four-wave superposition

$$
\begin{aligned}
I_o(k,l,t) = [&A_1(k,l,t) e^{2\pi i(m_c k/M + n_c l/N)} \\
+ &A_2(k,l,t) e^{2\pi i(-m_c k/M + n_c l/N)} \\
+ &A_3(k,l,t) e^{2\pi i(-m_c k/M - n_c l/N)} \\
+ &A_4(k,l,t) e^{2\pi i(m_c k/M - n_c l/N)}] e^{2\pi i w_c t/T} + \text{c.c.},
\end{aligned}
$$

$$(14)$$

which is the discrete analog of Eqs. (1) and (2) without higher-order terms, is considered as our basic oblique pattern
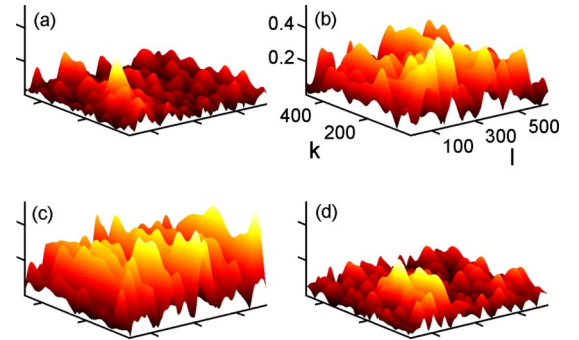

FIG. 5. (Color online) 3D plots of (a) $|A_1|$, (b) $|A_2|$, (c) $|A_3|$, and (d) $|A_4|$ for $t = 20\,009$; see Fig. 3(c) for the corresponding snapshot of I_o. The maxima are 0.34, 0.48, 0.53, and 0.31 for $|A_1|$, $|A_2|$, $|A_3|$, and $|A_4|$, respectively. Same tick labels and axis labels in all four plots.

created in the Hopf instability. In Fig. 5 snapshots of the $|A_j|$ at $t = 20\,009$ are shown; see Fig. 3(c) for the corresponding oblique pattern snapshot.

As mentioned in Sec. IV A, the pattern I, displayed in Fig. 2(a) for $t = 20\,009$, is not the "true pattern" generated by the fluid flow since it contains relatively large contributions from the second harmonics caused by nonlinearities of the shadowgraph method [11,40], as well as remnants after flatfielding near the center (0,0). For validating representation (14), we have doubled the size of the window used for filtering out the oblique modes in each direction, and computed the resulting oblique pattern $\tilde{I}$ for a sample of t values. For all of these values the relative norm difference $\|\tilde{I} - I_o\| / \|\tilde{I}\|$ was below 1%.

V. DIAGNOSIS OF THE ENVELOPE DYNAMICS

In this section we apply several diagnostic tools to the envelopes in order to characterize the dynamics quantitatively and qualitatively, and show that the pattern we study exhibits the characteristics of extensive spatiotemporal chaos. The methods applied comprise the calculation of mean intensities and spatial and temporal correlations, Karhunen-Loève decompositions in Fourier space and physical space, the location of holes of the envelopes in time and space, the identification of coherent vertical structures, and estimates of Lyapunov exponents using embedding techniques, and the analysis of basic wave patterns.

As can be seen in a movie [see Fig. 3(c) for a snapshot], the main characteristics of our pattern are patches of high intensity, separated by regions of low intensity. The form of the pattern within a patch changes, and the patches themselves split and merge permanently. The dominant envelopes contributing to the dynamics are A_3 and A_2, whereas A_1 and A_4 play the role of a kind of "background noise" (much lower intensity). Traveling stripes and rectangles are observed occasionally in small regions, mostly composed of right zig and zag waves corresponding to large values of $|A_3|$ and/or $|A_2|$. For example, in Fig. 3(c) we see a few almost perfect zag stripes, but the majority of the stripes are modulated. We can also see a few small patches with rectangular structure. Due to the dominance of A_2 and A_3, the rectangles are mainly traveling to the right. Overall the pattern appears spatiotemporally chaotic.

Another characteristic feature of our pattern is that the high-intensity patches appear confined to approximately vertical regions, as apparent in Fig. 3(c). These regions can also be recognized in the plots of $|A_3|$ and $|A_2|$ in Fig. 5. The calculations in Sec. V A show that on average the contribution from A_3 is higher than the contribution from A_2. Thus the dominant envelope is the zag-right envelope A_3.

A. Mean intensities and spatial autocorrelations

In Fig. 6(a) we show the temporal averages $\langle |A_j|^2 \rangle$ of the intensities of the envelopes. As apparent from this figure, the zag-right envelope A_3 has the highest mean intensity followed by the zig-right envelope A_2, whereas the left zig and zag envelopes A_4 and A_1 have consistently small mean inten-
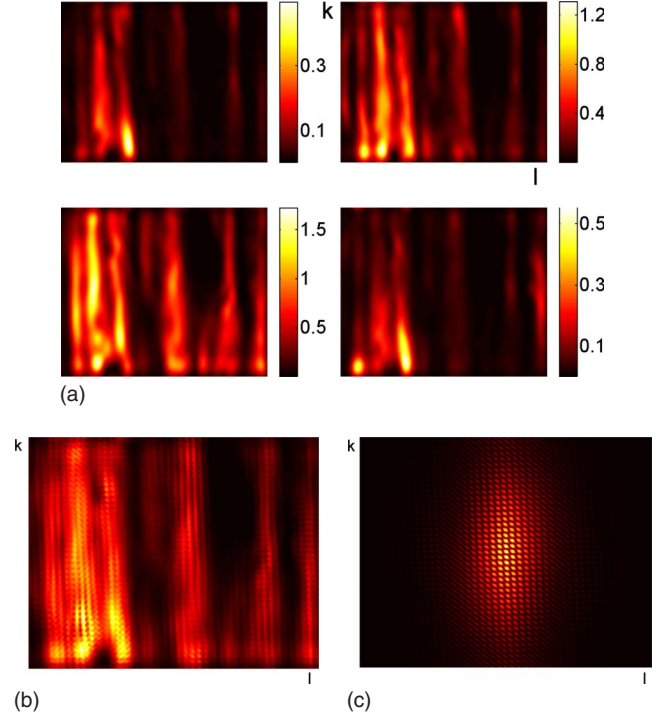

FIG. 6. (Color online) (a) Average intensities $\langle |A_1|^2 \rangle$ (upper left panel), $\langle |A_2|^2 \rangle$ (upper right panel), $\langle |A_3|^2 \rangle$ (lower left panel), and $\langle |A_4|^2 \rangle$ (lower right panel). Same axis labels in all four plots. (b) Mean-square oblique pattern $\langle (I_o)^2 \rangle$, and (c) spatial autocorrelation function $S_a[I_o]$ of the oblique pattern.

sities except at isolated spots. For all four envelopes we can recognize alternating approximately vertical active and inactive regions of high and low intensities, and the regions with highest intensities are located in left part of the cell.

By using Eq. (14), the mean intensity of the oblique pattern I_o can be decomposed as $\langle I_o^2 \rangle = \langle I_o^2 \rangle_{\text{slow}} + \langle I_o^2 \rangle_{\text{fast}}$, with the slow and fast components given by

$$2 \langle I_o^2 \rangle_{\text{slow}} = \sum_{j=1}^{4} \langle |A_j|^2 \rangle, \tag{15}$$

$$2 \langle I_o^2 \rangle_{\text{fast}} = (\langle A_1 \bar{A}_2 \rangle + \langle \bar{A}_3 A_4 \rangle) e^{4\pi i m_c k / M} + (\langle A_1 \bar{A}_4 \rangle$$
$$+ \langle A_2 \bar{A}_3 \rangle) e^{4\pi i n_c l / N} + \langle A_1 \bar{A}_3 \rangle e^{4\pi i (m_c k / M + n_c l / N)}$$
$$+ \langle \bar{A}_2 A_4 \rangle e^{4\pi i (m_c k / M - n_c l / N)} + \text{c.c.} \tag{16}$$

The full mean intensity $\langle I_o^2 \rangle$ is displayed in Fig. 6(b). This intensity pattern is dominated by $\langle I_o^2 \rangle_{\text{slow}}$, which shows again vertical regions of high and low intensities. There are two patches with highest intensity located in the left part of the cell. In the plot of $\langle I_o^2 \rangle_{\text{fast}}$ (not shown), we see mainly vertical stripes due to the fourth term in Eq. (16), some of which are modulated due to the first two terms in Eq. (16), as well as some short oblique stripes due to the last two terms in Eq. (16).

In order to quantify the spatial correlations, we have computed the spatial autocorrelation functions of the envelopes, defined by

$$S_a[A_j] = \langle \mathcal{F}_s^{-1}[|\mathcal{F}_s[A_j]|^2] \rangle.$$

The moduli of all four autocorrelation functions (not shown) have anisotropic, bell-shaped forms centered at (0,0). The associated horizontal and vertical correlation lengths are 50, 56, 70, and 49 and 112, 125, 146, and 105 pixels for $j=1,2,3$, and 4, respectively. Thus there is a significantly higher correlation in the vertical than in the horizontal direction, suggesting that the extensiveness of the chaos is dominant in the horizontal, transverse to the director, direction.

In terms of the $S_a[A_j]$, the spatial autocorrelation function $S_a[I_o]$ of the oblique pattern can be represented as

$$
\begin{aligned}
S_a[I_o](k,l) = {} & S_a[A_1](k,l)e^{2\pi i(m_c k/M + n_c l/N)} \\
& + S_a[A_2](k,l)e^{2\pi i(-m_c k/M + n_c l/N)} \\
& + S_a[A_3](k,l)e^{2\pi i(-m_c k/M - n_c l/N)} \\
& + S_a[A_4](k,l)e^{2\pi i(m_c k/M - n_c l/N)}.
\end{aligned}
$$

This function is displayed in Fig. 6(c); its pattern is a superposition of zig and zag stripes, with the zag stripes dominating. The different correlations in the vertical and horizontal directions can be clearly seen in this figure.

B. Karhunen-Loève decomposition

The mean intensities and autocorrelation functions allow identification of spatial regions with high and low activities and their correlations on average. However they do not provide information about the spatiotemporal complexity of the pattern, in particular the dimensionality, that is, the number of active degrees of freedom contributing to the dynamics. A method for objectively diagnosing the complexity of a spatiotemporal pattern is the Karhunen-Loève decomposition (KLD). This decomposition is a long-used technique in the signal analysis and processing. Unlike other techniques of decomposition that deal with fixed basis functions, the goal of a KLD is to find a minimal set of spatial modes that best fit the statistical features (variances) of the ordered state pattern, as well as uncover essential information about the dynamics of the system.

From a data-reduction point of view, the KLD is a statistical method for compressing spatiotemporal data by projecting them onto uncorrelated subspaces of decreasing variance. The basis functions spanning these subspaces are referred to as KLD eigenmodes. Here we apply the method to the time series of the spatial Fourier modes of all four envelopes simultaneously. In Sec. V E the KLD is applied to each envelope in physical space individually.

Writing the mean-subtracted time series of the nonzero spatial Fourier modes of A_j as rows in a matrix, and concatenating the resulting four matrices, yields a complex $4M_w N_w \times T$ data matrix $X = X(q,t)$, whose row index t labels time, and whose column index q encodes Fourier mode numbers (m,n) and envelope labels j. The KLD method consists of calculating the orthonormal eigenvectors $\psi_i = \psi_i(q)$ along with their eigenvalues λ_i of the autocorrelation matrix XX^* (the asterisk denotes the adjoint matrix), which satisfy

$$(XX^*)\psi_i = \lambda_i \psi_i.$$

The eigenvalues are real and non-negative and are sorted by magnitude, $\lambda_1 \geq \lambda_2 \geq \cdots \geq \lambda_{4M_w N_w} \geq 0$. In terms of the ψ_i and the orthonormal temporal eigenvectors $\phi_i = \phi_i(t)$, which satisfy $(X^* X)\phi_i = \lambda_i \phi_i$, the data matrix can be represented as

$$X(q,t) = \sum_{i=1}^{4M_w N_w} \sqrt{\lambda_i}\,\psi_i(q)\phi_i^*(t).$$

Statistically, the eigenvalue λ_i represents the (temporal) variance of the data in the direction ψ_i, and the data projected onto different eigenvectors are uncorrelated. The fraction of the total variance contained in the projection onto ψ_i is measured by the normalized eigenvalue $\tilde{\lambda}_i = \lambda_i / \Sigma_j \lambda_j$. Given a prescribed fraction $r \leq 1$, an optimal reconstruction of the data, in the sense that they are projected onto a space of minimal dimension and that the projected data capture at least the fraction r of the total variance, is given by

$$X^{\mathrm{rec}}(q,t) = \sum_{i=1}^{D} \sqrt{\lambda_i}\,\psi_i(q)\phi_i^*(t),$$

where

$$D = \min\left\{ d \,\Big|\, \sum_{i=1}^{d} \tilde{\lambda}_i \geq r \right\} \equiv D_{\mathrm{KLD}}(r).$$

In practice one fixes a "reasonable" value of r, typically $r = 0.9$, and considers $D_{\mathrm{KLD}}(r)$ as intrinsic dimension of the data. In [41–43], $D_{\mathrm{KLD}}(r)$ has been defined as KLD dimension of the system.

In Fig. 7(a) the first 70 normalized KLD eigenvalues $\tilde{\lambda}_i$ are displayed as functions of the KLD mode number i, together with the fraction of the variance, $\Sigma_{j=1}^{i} \tilde{\lambda}_j$, captured by all KLD modes with mode numbers $\leq i$. In order to reproduce 90% of the variance, 45 KLD modes are needed $[D_{\mathrm{KLD}}(0.9) = 45]$. Thus we are dealing with a high-dimensional, complex pattern that cannot be described by a chaotic dynamical system with few degrees of freedom. The first three modes contain 18%, 10%, and 7% of the total variance, and the mode with mode number 40 contains 0.34%. Although this is small, this mode cannot be neglected if a reconstruction with 90% variance is required.

Each KLD mode $\psi_i(q)$ is composed of four envelope components $A_1, \ldots, A_4$ in Fourier space. The L_2 norms of these components (with $\|\psi_i\| = 1$) are plotted in Fig. 7(b) as functions of i. The moduli of the first mode are visualized in Fig. 8(a), with the Fourier modes of $A_1, \ldots, A_4$ displayed in separate cells.

As apparent from Fig. 7(b), the first two KLD modes are dominated by A_3, with only small contributions from A_1, A_2, A_4. The third mode is dominated by A_2, but there is also a significant contribution from A_3. For $i \leq 44$, 32, 11, and 1 modes are dominated by A_3, A_2, and A_4, respectively. The contributions from A_1 and A_4 are small for $i \leq 10$ and get larger when i increases, until eventually the L_2 norms of all four envelopes fluctuate about 0.5. Moreover, plots analo-
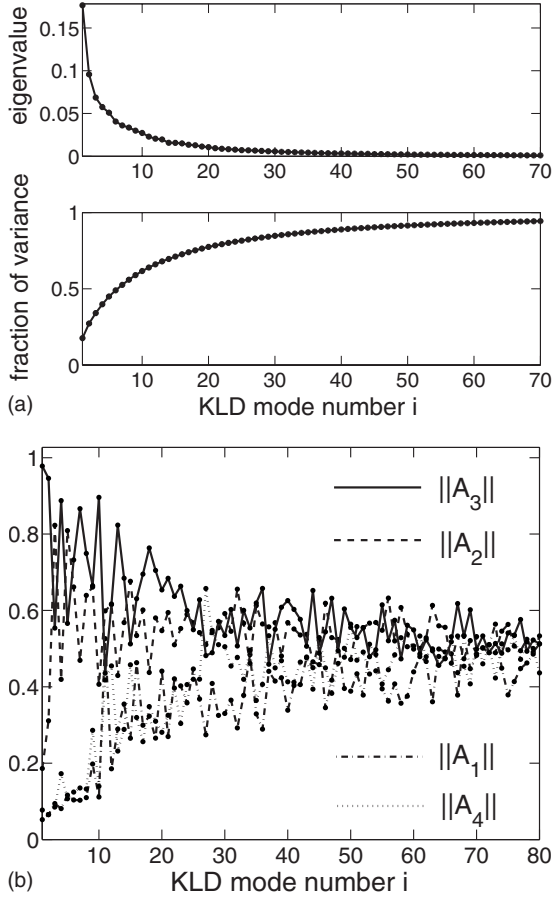
FIG. 7. (a) First 70 normalized KLD eigenvalues (upper panel) and fraction of variance captured by KLD modes up to mode number i (lower panel) versus i resulting from a KLD applied to the $4 \times 17 \times 34$ slow Fourier modes of $A_1, \ldots, A_4$ simultaneously. Needed are 45 modes to capture 90% variance. (b) L_2 norms of the envelope components $A_1, \ldots, A_4$ of the (normalized) KLD modes $\psi_i(q)$ versus mode number i. Solid, dashed, dashed-dotted, and dotted lines are for $\|A_3\|$, $\|A_2\|$, $\|A_1\|$, and $\|A_4\|$, respectively.

gous to Fig. 8(a) show that the distributions in Fourier space become broader and more irregular when i increases.

By Fourier inversion, the envelope components of the KLD modes in Fourier space can be transformed to "eigenenvelopes" in physical space. The moduli of the eigenenvelopes computed from the first KLD mode $\psi_1(q)$ are shown in Fig. 8(b). They are dominated by A_3, and $|A_3|$ is highest in the left part of the cell. The eigenenvelopes for the second mode (not shown) are also dominated by A_3, and here we see high-intensity regions in the right part of the cell. For both modes the high-intensity regions are extended in the vertical direction, consistent with the mean intensity plot of Fig. 6(a). Apparently the KLD has identified the two parts of the cells as uncorrelated components for A_3. The third eigenenvelope (not shown) is dominated by A_2, and exhibits a single vertical compartment with high values of $|A_2|$. For $i=4$ (not shown; A_3 dominant), we find a single high-intensity spot for A_3 in the left part of the cell. For $i=5$ (also not shown), A_2 and A_3 have comparable contributions, and here we find several vertical high-intensity regions for A_3 in both left and right parts of the cell, whereas A_2 shows only
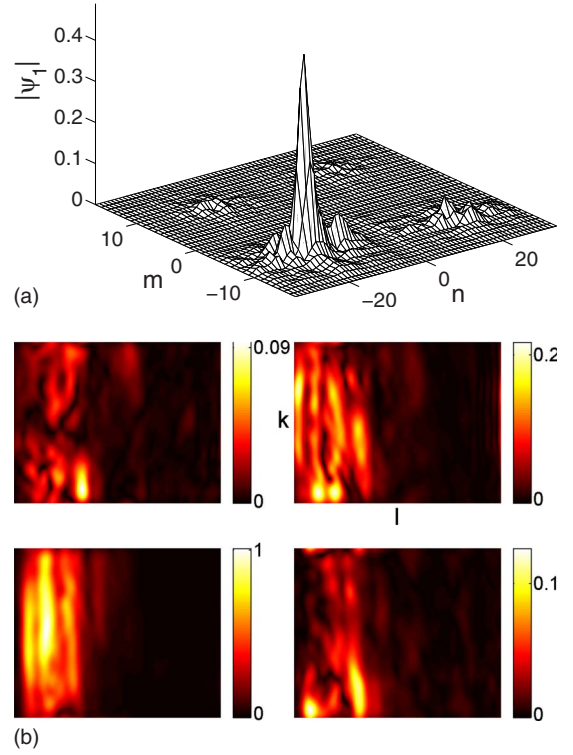

FIG. 8. (Color online) (a) Moduli of the first KLD mode $\psi_1(q)$ displayed in four cells of size 17×34, with the Fourier modes of A_1, A_2, A_3, and A_4 placed in $(m>0, n>0)$, $(m<0, n>0)$, $(m<0, n<0)$, and $(m>0, n<0)$, respectively. (b) Moduli of the eigenenvelopes of A_1 (upper left panel), A_2 (upper right panel), A_3 (lower left panel), and A_4 (lower right panel) in physical space for the first KLD mode. Same axis labels in all four plots.

two such regions in the left part of the cell. Generally, the high-intensity regions of the eigenenvelopes are significantly more extended in the vertical than in the horizontal direction.

In Fig. 9(a) the moduli of the temporal eigenfunctions $\phi_i(t)$ are shown for $i=1,2,3,40$. A characteristic feature of these eigenfunctions is that the number of approximative zeros of $|\phi_i(t)|$ increases with increasing i. Phase plots of two or three temporal eigenfunctions, e.g., $|\phi_1|$ versus $|\phi_2|$, do not reveal any discernible structure.

Owing to representation (14), the spatial KLD eigenpatterns $I_{o,i}$ of the oblique pattern I_o can be represented as

$$
\begin{aligned}
I_{o,i}(k,l) = {} & A_{1,i}(k,l)e^{2\pi i(m_c k/M + n_c l/N)} + A_{2,i}(k,l)e^{2\pi i(-m_c k/M + n_c l/N)} \\
& + A_{3,i}(k,l)e^{2\pi i(-m_c k/M - n_c l/N)} \\
& + A_{4,i}(k,l)e^{2\pi i(m_c k/M - n_c l/N)},
\end{aligned}
$$

where the $A_{j,i}(k,l)$ are the eigenenvelopes computed from $\psi_i(q)$. The eigenpatterns for $i=1,2,3,40$ are shown in Fig. 9(b). For $i=1,2$ and $i=3$ we see vertical high-intensity regions with zag waves and zig waves due to the dominance of A_3 and A_2, respectively. When i increases, the eigenpatterns develop more and more patches of high intensity with superpositions of zig and zag waves; see Fig. 9(b) for $i=40$.
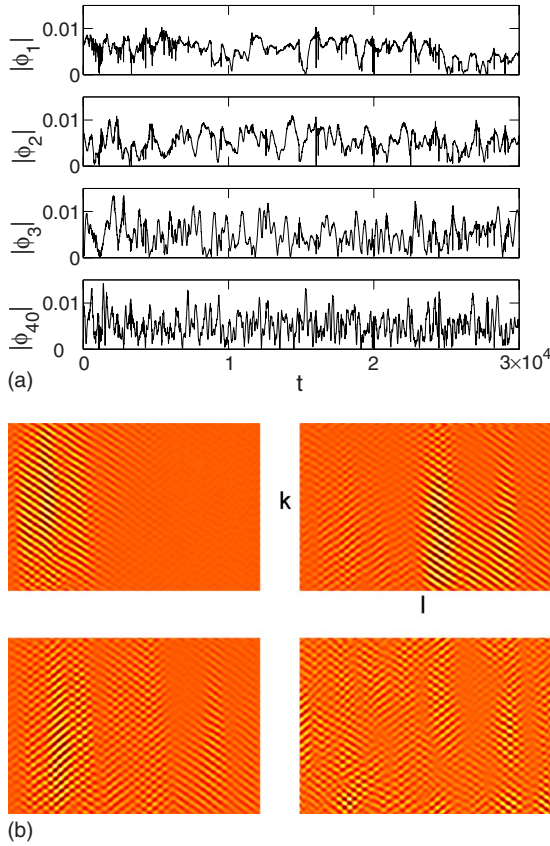
FIG. 9. (Color online) (a) Moduli of the temporal KLD eigenfunctions $\phi_i(t)$, and (b) moduli of the oblique eigenpatterns associated with the eigenenvelopes, for KLD mode numbers $i=1,2,3,40$ (upper left, upper right, lower left, and lower right panels). Same axis labels for all four plots in (b).

C. Holes

The 1D complex Ginzburg-Landau equation admits special so-called hole-solutions [44], which are localized solutions with a very small value of the modulus at a distinguished spatial location. In simulations of the Ginzburg-Landau equation, one can observe several such holes moving through space, merging and disappearing, or being created [45,46]. We have made similar observations in simulations of the four coupled Ginzburg-Landau equations describing the oblique oscillatory instability in 2D anisotropic systems [19,20,22], and the envelopes extracted from our experimental pattern also appear to exhibit a number of holes, as can be seen in the snapshot in Fig. 5(a).

Since the appearance of holes is a characteristic feature of the envelope dynamics, we study and visualize their location and distribution. To compute them at a given instant of time, we consider the pixel values of an envelope as values of a continuous function on a rectangular $M \times N$ grid, and use a bilinear interpolation to represent this function in each basic rectangle. The hole positions are then identified with the grid points (k,l) that are nearest to the simultaneous zeros of the real and imaginary parts of the interpolated function.

For each envelope A_j, the statistics of the holes is described by the holes' frequency distribution $F_{h,j}(k,l)$, which we define as the number of times a hole occurs at the posi-
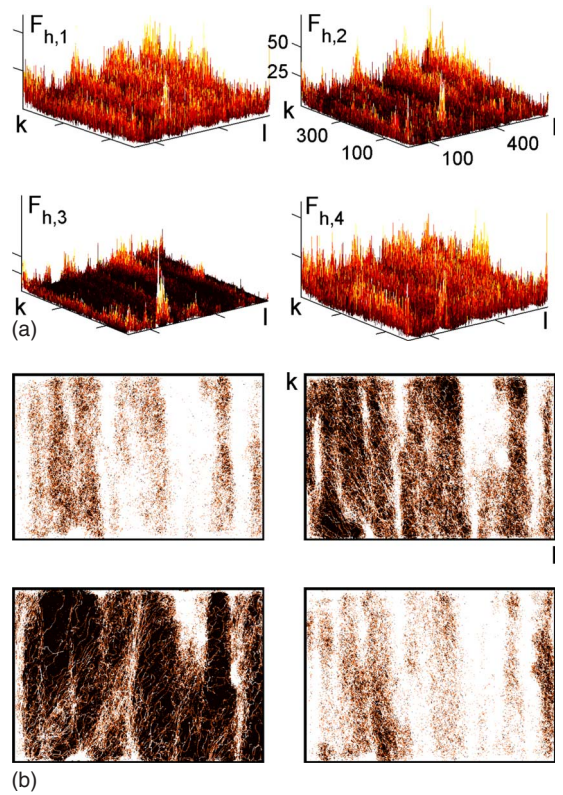

FIG. 10. (Color online) (a) Holes' frequency distributions $F_{h,j}$ of the envelopes A_j, with $1 \le j \le 4$. The maxima are 62, 77, 138, and 60 for $j=1,2,3$, and 4. Same tick labels for all four plots. (b) Reduced plots of $F_{h,j}$ (upper left, upper right, lower left, and lower right panels for $j=1,2,3$, and 4), with locations where no holes, one hole, and two or more holes occur plotted black, gray (brown online), and white, respectively. The fractions of the black and gray (brown online) areas in percent are 7.9, 34.5, 61.8, and 7.7 and 12.1, 19.9, 15.3, and 11.4 for $j=1,2,3$, and 4. Same axis labels for all four plots.

tion (k,l). Three-dimensional plots of these distributions are shown in Fig. 10(a). As can be seen in this figure, A_1 and A_4 have significantly more holes than A_2 and A_3, and their holes' frequency distributions are more irregular. Moreover, all four distributions appear to be organized in approximately vertical regions of alternating high and low numbers of holes. Reduced 2D plots of these distributions are shown in Fig. 10(b), with locations where no hole, one hole, and two or more holes occur plotted black, gray (brown online), and white, respectively. We can see relatively large and contiguous black regions in the plots for $F_{h,2}$ and $F_{h,3}$, whereas most of the area in the plots for $F_{h,1}$ and $F_{h,4}$ is white. The gray (online red) line segments within the dark regions in the plots for $F_{h,2}$ and $F_{h,3}$ mark single hole trajectories. The vertical averages of these distributions are shown in Fig. 12(c).

Time plots of the holes are displayed in Fig. 11. In Fig. 11(a) the instantaneous number of holes of A_j in the cell, $N_{h,j}(t)$, is plotted as function of t over the full time range. Notice the few isolated high peaks in these time series, which occur simultaneously for two or three envelopes. Summing up the time series yields 1.6×10^6, 0.9×10^6, 0.4×10^6, and 1.6×10^6 as total numbers of holes exhibited by A_j for $j=1$, 2, 3, and 4.
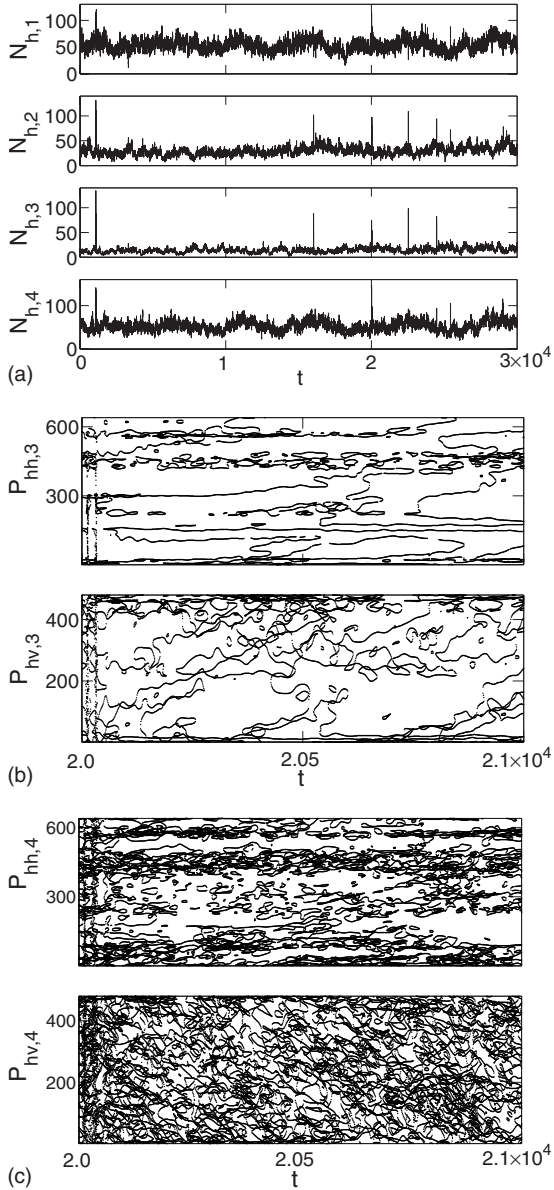
FIG. 11. (a) Number $N_{h,j}$ of holes of A_j in the cell versus time. [(b) and (c)] Horizontal (upper panel) and vertical (lower panel) positions of holes versus time for (b) A_3 and (c) A_4. Time range: $20\,000 \leq t \leq 21\,000$.

In the top and bottom panels of Figs. 11(b) and 11(c), the horizontal (l) and vertical (k) positions of the holes of A_3 and A_4 are plotted as functions of t in the range $20\,000 \leq t \leq 21\,000$. For A_3 we can see narrow horizontal intervals populated by many holes. Between these intervals only few mostly contiguous hole trajectories are present. In the vertical direction, A_3 shows more holes in the upper half of the cell than in the lower half, which is also apparent in the $F_{h,3}$ plot of Fig. 10(b). For A_4, the vertical direction is densely and almost uniformly populated by holes, whereas in the horizontal direction there are regions that are not covered by hole trajectories over certain time ranges. The hole trajectories of A_2 (not shown) are similar to those of A_3 in the horizontal direction, but more uniform and dense in the vertical direction. For A_1 (also not shown) the trajectories are

similar to those of A_4. The percentages of the numbers of grid points populated by holes of A_j at least once are 92.14, 65.54, 38.23, and 92.31 for $j=1$, 2, 3, and 4.

D. Temporal correlation analysis and coherent vertical structures

One of the most striking features of our pattern is the appearance of high-intensity patches of the envelopes, which are confined to approximately vertical rigid regions. We identify the envelope patterns within these regions with coherent vertical structures, and the regions themselves with regions of coherence. In order to determine their boundaries, we study the temporal correlations of the envelopes in the horizontal direction.

To reduce the computational effort of this correlation analysis, the spatial domain is partitioned into 32×128 cells of size 15×5 pixels, and the A_j are represented by the spatial averages over these cells, which is justified by their slow spatial variation. We denote these local averages by $a_j(k,l,t)$, where here $1 \leq k \leq 32$ and $1 \leq l \leq 128$ are the vertical and horizontal cell labels.

Since our goal is to quantify temporal correlations in the horizontal direction, we make a further reduction by representing A_j in each vertical bin with label l by a single time series $\varphi_j(l,t)$. This time series is determined through a KLD of a_j in each bin, resulting in 32 temporal KLD modes $\varphi_{ji}(l,t)$, with $1 \leq i \leq 32$. To capture 90% of the variance, 8–11, 6–10, 6–8, and 8–11 modes are needed at the different sites for $j=1$, 2, 3, and 4, and the first mode contains 20–40% and 30–50% of the variance of a_1, a_2, a_4, and a_3, respectively. The first mode, $\varphi_j(l,t) \equiv \varphi_{j1}(l,t)$, is used in the temporal correlation analysis.

Given any two time series $u(t)$ and $v(t)$, the normalized cross-correlation function $C_{uv}(t)$ is given by

$$C_{uv}(t) = \frac{\mathcal{F}_t^{-1}[\mathrm{Re}\{\mathcal{F}_t[u]\overline{\mathcal{F}_t[v]}\}](t)}{\|u\|\|v\|},$$

where $\|u\|$ and $\|v\|$ are the L_2 norms of u and v. A measure of the correlation between $u(t)$ and $v(t)$ is provided by the cross-correlation coefficient, defined as

$$C[u,v] = \max_t |C_{uv}(t)|.$$

Note that $0 \leq C[u,v] \leq 1$ and $C[u,v]=1$ if and only if v is related to u by a time shift and a scalar multiplication.

To quantify the temporal correlations in the horizontal direction, we compute for each envelope A_j the matrix $C_{H,j}$ of horizontal cross-correlation coefficients associated with the dominant vertical KLD modes,

$$C_{H,j}(l,l') = C[\varphi_j(l,.), \varphi_j(l',.)],$$

which is a positive and symmetric 128×128 matrix with maximal value of 1 in the diagonal. This matrix is displayed in Fig. 12(a) for each j. As expected, there is little correlation between vertical bins at sites l and l' that are sufficiently apart from each other. The thickened light regions around the diagonal correspond to bins l with high correlations to neighboring bins.
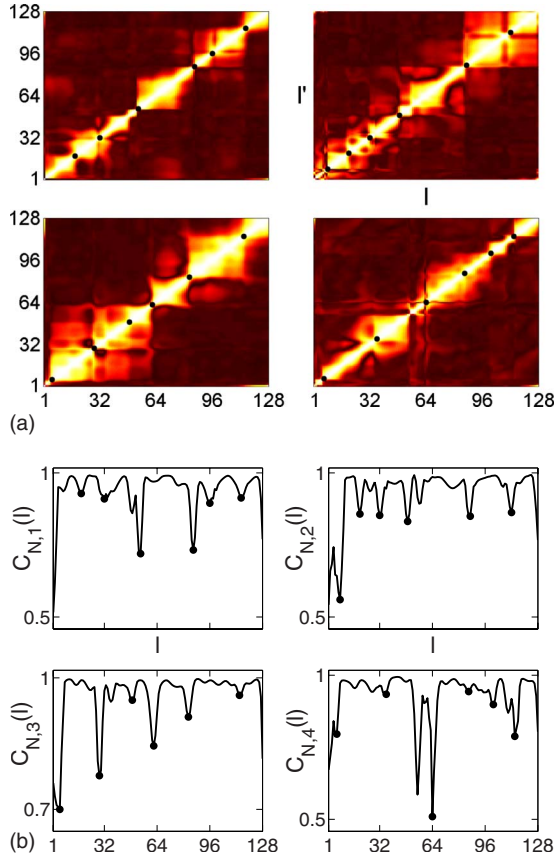
FIG. 12. (Color online) (a) Horizontal cross-correlation coefficients $C_{H,j}(l,l')$ (upper left, upper right, lower left, and lower right panels for $j = 1, 2, 3$, and 4) of the 128 dominant KLD time series $\varphi_j(l,t)$ at horizontal position (vertical bin number) l, with $1 \le l \le 128$. In these calculations the envelopes A_j have been averaged over 5 and 15 pixels in the horizontal and vertical directions, respectively; see text for details. Same grayscale (color online) map, axis labels, and axis scales for all four plots; maximal value of 1 on the diagonal. (b) Nearest-neighbor correlation coefficients $C_{N,j}(l)$ obtained via averaging $C_{H,j}(l,l')$ over the five nearest neighbors l' of l. The dots in (a) and (b) mark boundaries between seven adjacent coherence regions for each envelope A_j, identified with the six steepest and sufficiently distant minima of $C_{N,j}$. Same horizontal axis labels and tick labels for all four plots.

Bins with small nearest-neighbor correlations are identified with separation boundaries between adjacent vertical coherence regions. To determine these boundaries, we calculate for each l the average correlation of $\varphi_j(l,t)$ and $\varphi_j(l',t)$ for $|l - l'| \le 2$, yielding the 1D array $C_{N,j}(l)$ of (average) nearest-neighbor correlation coefficients shown in Fig. 12(b). In this figure we can clearly recognize six distinguished minima of $C_{N,j}(l)$ for $j = 1, 2, 3$, which we select as separation boundaries. The graph of $C_{N,4}(l)$ is more complicated. Here we select six minima as separation boundaries by the condition that they are the steepest and sufficiently distant from each other. The selected minima are displayed by dots in Fig. 12(b) and on the diagonal in Fig. 12(a). Their bin labels are summarized in Table I(a).

Figure 13(a) shows the vertical averages $\langle |a_j|^2 \rangle_v$ of the intensities $|a_j|^2$ as functions of time and bin number, together

TABLE I. (a) Bin labels of the points displayed by dots in Figs. 12(a) and 12(b). These labels correspond to the boundaries separating the vertical coherence regions identified for each envelope. (b) Numbers of KLD modes required to capture 90% variance in KLDs of a_j restricted to the coherence regions 1–7 (left to right).

(a)

j	Bin labels					
1	18	32	54	86	96	115
2	8	20	32	49	87	112
3	5	29	49	62	83	114
4	6	36	64	86	101	114

(b)

j	$D_{\mathrm{KLD}}(0.9)$ in regions 1–7						
1	11	5	7	21	17	10	12
2	4	4	4	5	7	6	8
3	6	4	4	4	3	4	3
4	9	10	8	12	23	9	5

with the separation boundaries which are displayed by vertical white lines. To reduce the amount of data to be displayed, local temporal averages over 50 time steps are plotted. In Fig. 13(b) the mean intensities averaged over the vertical direction, $\langle \langle |A_j|^2 \rangle \rangle_v$, are shown, also together with the separation boundaries displayed by dashed lines. In both figures the coherence regions, computed through minimal temporal correlations, match well the active and inactive regions revealed in the intensity plots. As a further characteristic, we show in Fig. 13(c) the vertical averages of the holes' frequency distributions, $\langle F_{h,j} \rangle_v$. Here the boundaries between adjacent regions are located near peaks of these distributions.

To resolve the coherent structures in the vertical direction, we have performed a KLD of the a_j in each of the coherence regions 1–7. The numbers of KLD modes required to capture 90% of the variance in these regions are summarized in Table I(b). Notice that significantly fewer modes are needed for a_2 and a_3 than for a_1 and a_4. The primary coherent structures of the A_j can be identified with the first KLD modes in each of the coherence regions. Plots of their moduli (not shown) for the dominant envelopes A_3 and A_2 show that most of these modes are elongated in the vertical direction.

E. Diagnosis of spatiotemporal chaos

The most basic tool for analyzing a chaotic dynamical system is to compute its Lyapunov exponents, which measure the divergence of nearby trajectories. The knowledge of the spectrum of Lyapunov exponents enables one to estimate the number of active degrees of freedom in terms of the Lyapunov (or Kaplan-Yorke) dimension [47], as well as to approximate the Kolmogorov-Sinai entropy that quantifies the growth of uncertainty if the system is subject to perturbations [48]. For low-dimensional systems it is straightforward to compute the Lyapunov spectrum not only from model equations using the Jacobian, but also from measured
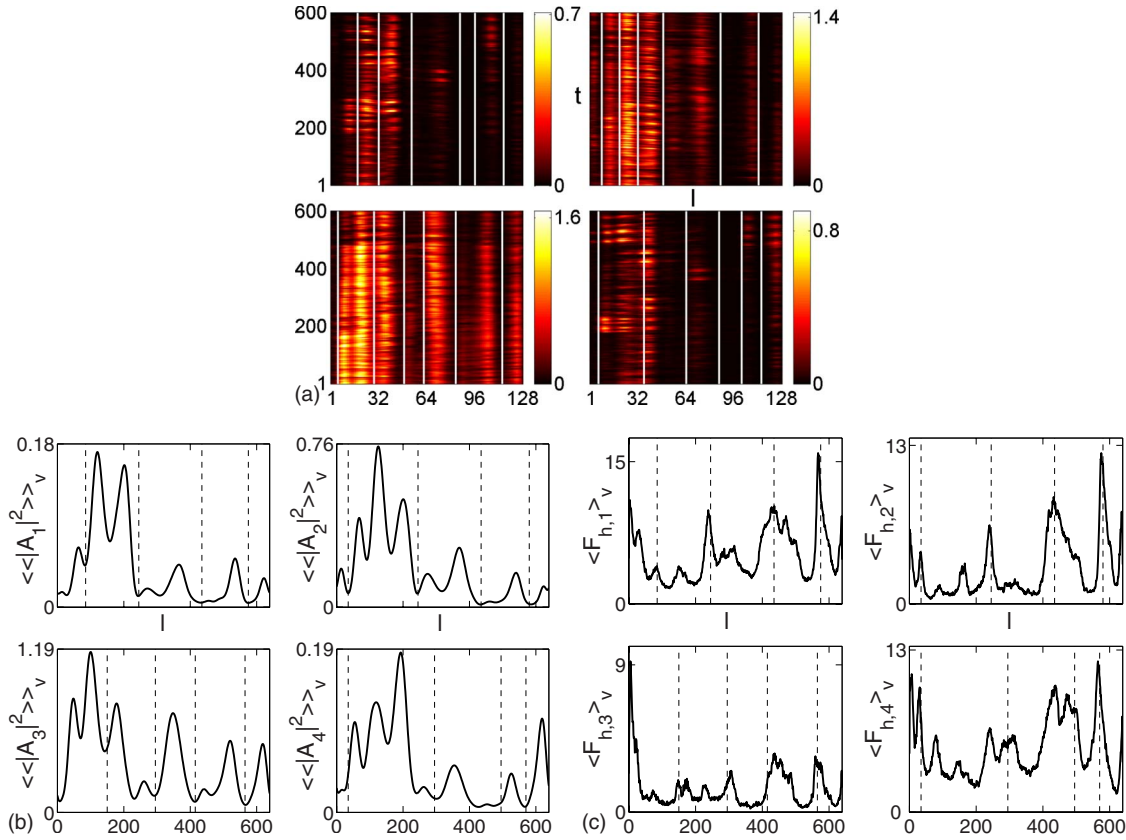
FIG. 13. (Color online) (a) Intensities $\langle|a_j|^2\rangle_v$ (upper left, upper right, lower left, and lower right panels for $j=1,2,3,4$) of the envelopes A_j averaged over vertical bins of widths of 5 pixels and 50 time steps. Horizontal and vertical axes represent bin numbers (1–128) and times ($0 \leq t/50 < 600$), respectively. Same axis labels and axis scales for all four plots. (b) Moduli of the spatial averages of the mean intensities $\langle|A_j|^2\rangle$ in the vertical direction. (c) Vertical averages $\langle F_{h,j}\rangle_v$ of the holes' frequency distributions $F_{h,j}$ shown in Fig. 10(a). Same horizontal axis labels and tick labels for all four plots in (b) and (c). The vertical lines, displayed white in (a) and dashed in (b) and (c), represent the separation boundaries corresponding to the dots marked in Figs. 12(a) and 12(b).

data using nonlinear time-series analysis methods based on embedding techniques.

For high-dimensional systems however, with many active degrees of freedom, the computation of Lyapunov spectra is problematic, even if governing equations are known [49,50]. Specifically in spatially extended systems there is the possibility of extensive spatiotemporal chaos, which means that the Lyapunov dimension, or other fractal dimensions, and more generally the spectrum of positive Lyapunov exponents scale linearly with the volume of the system and so become extensive quantities [51,52]. Such systems have to be characterized by an intensive quantity related to the intrinsic dimension of the system. A natural dynamical invariant of this kind is the Lyapunov dimension density, defined by $\delta_L = \lim_{V\to\infty} D_L/V$, where V is the system's volume and D_L is its Lyapunov dimension [51]. An equivalent measure is the associated correlation length $\xi_L = \delta_L^{-1/d}$, where d is the number of asymptotically large spatial dimensions ($d=2$ for our electroconvection pattern). To compute δ_L or ξ_L in practice requires computation of Lyapunov spectra for systems of increasing size [51,52]. This is, however, impractical for the analysis of experimental data, since the number of data needed in embedding calculations for estimating Lyapunov spectra grows exponentially with the system size if the sys-

tem is extensively chaotic. Therefore another approach is needed to test data for extensive chaos.

An approach that is based on the Karhunen-Loève decomposition and is straightforwardly applicable to experimental data was introduced by Zoldi and Greenside [53]; for its application to spiral defect chaos see [4]. The basic idea is that for extensive chaos the KLD dimension $D_{\mathrm{KLD}}(r)$ introduced in Sec. V B also behaves like an extensive quantity. That is, the rate of increase in $D_{\mathrm{KLD}}(r)$ with the volume V is similar to the rate of increase in D_L, since the extensivity of the dimension arises from the appearance of new orthogonal directions contributing to the dynamics when V increases. Thus the KLD correlation length, defined by

$$\xi_{\mathrm{KLD}}(r) = [D_{\mathrm{KLD}}(r)/V]^{-1/d},$$

should converge to a positive number when $V \to \infty$ if the system is extensively chaotic. Although $D_{\mathrm{KLD}}(r)$ is not a dynamical invariant like D_L, and is somewhat ambiguous because of its r dependence, a nonzero limit is an indicator of extensive chaos. It has been demonstrated [53] that the onset of extensivity of $D_{\mathrm{KLD}}(r)$ accurately predicts the onset of extensivity of D_L for increasing V.

We have applied the KLD first to the full system, that is, to all 32×128 time series $a_j(k,l,t)$ computed via local aver-
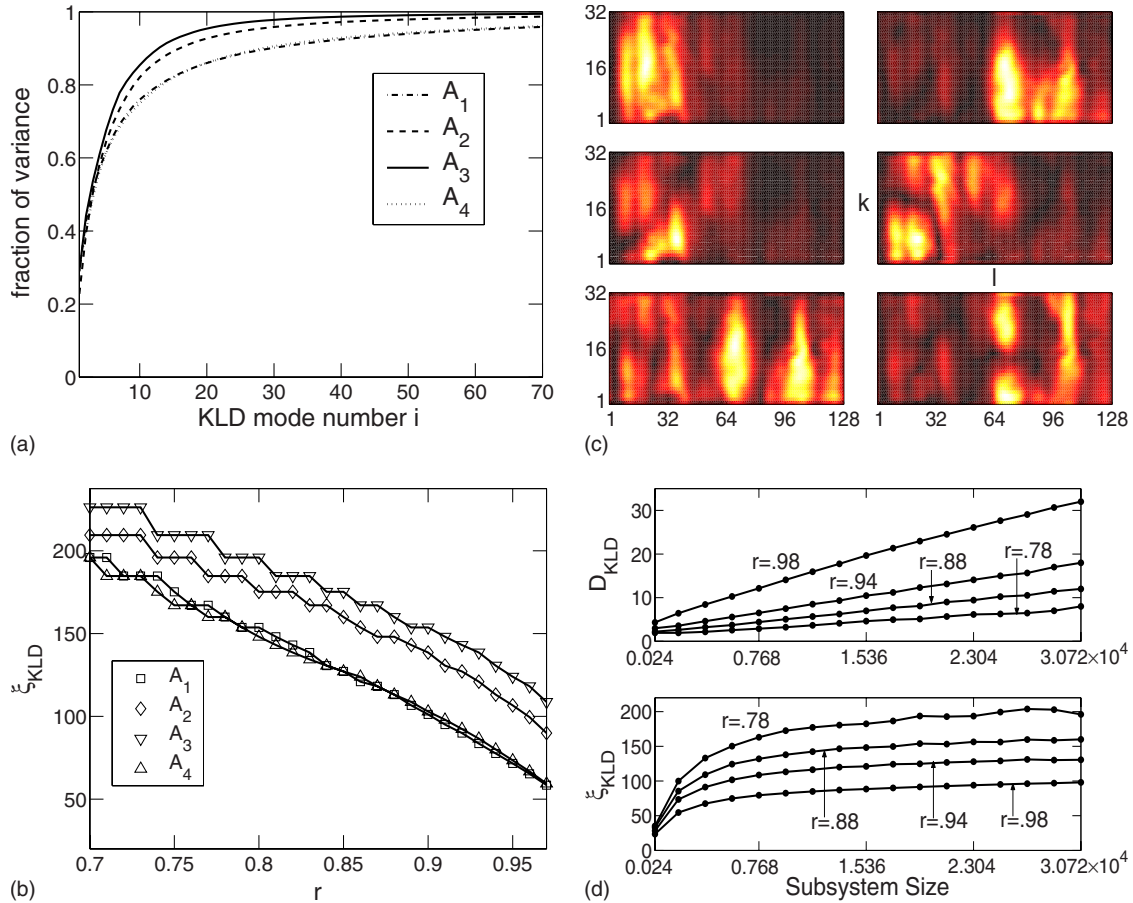
FIG. 14. (Color online) (a) Fraction of variance captured by KLD modes up to mode number i versus i, resulting from a KLD of each of $A_1, \ldots, A_4$ averaged over cells of size 15×5 pixels. (b) KLD correlation length $\xi_{KLD}(r)$ versus r calculated from the data displayed in (a). (c) First six spatial KLD modes for A_3. Axis labels (same for all six plots) represent horizontal and vertical cell labels. Same axis scales for all six plots. (d) Upper panel: KLD dimension $D_{KLD}(r)$ for four values of r calculated from local KLDs of A_3 in subsystems of increasing size versus subsystem size (area measured in pixels^2). Lower panel: $\xi_{KLD}(r)$ associated with $D_{KLD}(r)$. See text for details.

ages of each of the envelopes A_j. In Fig. 14(a) we show the fraction of the variance captured by the KLD modes with mode numbers $\leq i$ versus i. Notice that the variance curves for A_1 and A_4 are very close. The values of $D_{KLD}(0.9)$ are 30, 16, 13, and 29, yielding $\xi_{KLD}(0.9) = 101$, 139, 154, and 103 pixels for $j = 1, 2, 3,$ and 4.

In Fig. 14(b), $\xi_{KLD}(r)$ is displayed for a range of r values. The steps in this plot are due to small D_{KLD} values for smaller values of r [$D_{KLD}(0.7) = 6$ for A_3].

The first six eigenenvelopes for A_3 are shown in Fig. 14(c). We note that the first two of them are very similar to the first two A_3 modes calculated from the global KLD (Figs. 8 and 9). The third modes are different, because in the global KLD this mode is dominated by A_2.

To diagnose extensive chaos, we have performed a KLD for A_3 in subsystems of increasing size. A subsystem with an area of $75 \times 32 \times L$ pixels^2 is identified with the time series $a_3(k, l, t)$ for $1 \leq k \leq 32$ and $l_0 + 1 \leq l \leq l_0 + L$. For $L < 128$ we have varied l_0 over the accessible range and calculated the averages of $D_{KLD}(r)$ and $\xi_{KLD}(r)$. Four values of r have been chosen: $r = 0.78, 0.88, 0.94,$ and 0.98. The KLD dimensions $D_{KLD}(r)$ and the associated correlation lengths $\xi_{KLD}(r)$ for these r values are displayed in the top and bottom panels of

Fig. 14(d) as functions of the area. For the three larger values of r we can clearly see that $D_{KLD}(r)$ scales linearly with the area, and $\xi_{KLD}(r)$ approaches a constant value, which suggests that we have extensive chaos.

The limiting values of $\xi_{KLD}(r)$ are 196, 160, 131, and 98 pixels for $r = 0.78, 0.88, 0.94,$ and 0.98. Recall that the horizontal and vertical correlation lengths for A_3 (Sec. V A) are 70 and 146 pixels, respectively. Their geometric mean is 101, which is close to the limiting value of 98 of $\xi_{KLD}(r)$ for $r = 0.98$. Furthermore, the ratio $640/98 \approx 6.53$ matches number 7 of coherence regions identified in Sec. V D. Thus the numerical values resulting from the three different diagnostic methods are consistent.

Next we consider the first (largest) Lyapunov exponent, λ, which is not an extensive quantity [54]. We did a number of embedding calculations, trying to estimate λ for different embedding dimensions d_e and several time series, including various slow Fourier modes, vertical averages of the envelopes, and the first vertical KLD modes $\varphi_j(l, t)$ exploited in Sec. V D. For all time series considered, λ increased with d_e for $1 \leq d_e \leq 3$, and for $d_e > 3$ we observed mild fluctuations for $4 \leq d_e \leq 6$, and a relatively strong increase with d_e for $d_e > 6$. False-nearest-neighbor tests showed an increase in
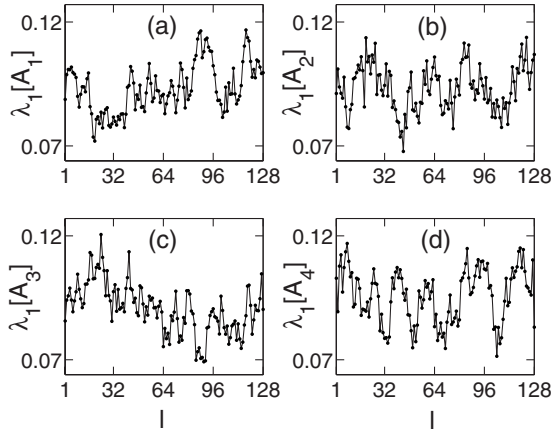
FIG. 15. First Lyapunov exponents for A_j, $\lambda_1[A_j]$ ($1 \leq j \leq 4$), estimated from the real parts of the 128 dominant KLD time series $\varphi_j(l,t)$ defined in Sec. V D versus l, with $1 \leq l \leq 128$, using embedding dimension of 4 and delay of 100.

the number of false nearest neighbors with increasing d_e in the range $d_e > 6$, but did not indicate the presence of false nearest neighbors for $d_e \leq 6$. Optimal delays turned out to be about 100–150; these large values are due to the slow variation in the time series. The estimated values of λ for $4 \leq d_e \leq 6$ varied between 0.05 and 0.13.

The outcome of these calculations for $d_e = 4$ and delay of 100 is displayed in Fig. 15 for the real parts of the first vertical KLD modes $\varphi_j(l,t)$ for $1 \leq l \leq 128$ and all four envelopes. The fluctuations of λ with l are relatively strong; the mean values are

$$0.0933 \pm 0.0100, \quad 0.0933 \pm 0.0094,$$

$$0.0907 \pm 0.0100, \quad \text{and} \quad 0.0957 \pm 0.0108$$

for $j = 1$, 2, 3, and 4. The mean value over all four envelopes is 0.0933 ± 0.0102. Because of the problems encountered in embedding calculations for high-dimensional chaotic systems, this mean value cannot be considered as approximation of the true Lyapunov exponent, but rather as lower bound. In model calculations it has been observed that the largest Lyapunov exponent increases with increasing system size toward a finite value, and that the Lyapunov exponents of two consecutive sizes are interleaved; see, e.g., [52,55]. Qualitatively our estimates of the first Lyapunov exponent confirm the chaoticity of the pattern, and together with the KLD calculations for increasing subsystem size, they strongly suggest that we have extensive spatiotemporal chaos.

A further approach to diagnosing spatiotemporal chaos was suggested by Jung *et al.* [56], which is based on a decomposition of the spatiotemporal pattern into coherent space-time clusters. In this approach the space-time cube is first thresholded to distinguish between active and inactive sites, and then the active sites are decomposed into contiguous regions referred to as coherent clusters. The size s of each of the coherent clusters is the number of active sites constituting the cluster, and is characterized by a cluster-size distribution $p(s)$. We have done this analysis for the intensity $|a_3(k,l,t)|^2$ using a threshold value of 0.7 (the maximum of
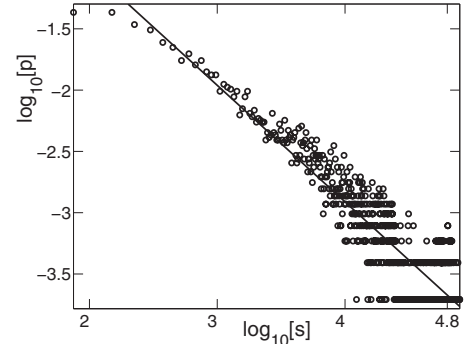

FIG. 16. Logarithmic plot of cluster size distribution $p(s)$ for a_3 (threshold, 0.7) versus cluster size s in pixels^2. In the linear range $p(s)$ can be approximated by the power law bs^α with an exponent $\alpha \approx -0.95$.

$|a_3|^2$ is 1.96). The resulting cluster-size distribution is shown in Fig. 16 on a logarithmic scale, suggesting a power-law distribution $p(s) = bs^\alpha$ with an exponent $\alpha \approx -0.95$, which is indicative of disordered spatiotemporal behavior [56]. The exponent depends on the threshold. For the threshold values of 0.6 and 0.8 the exponents turned out to be -0.85 and -1.02, respectively.

F. Pattern analysis

According to [23,24], the normal form for the oblique Hopf instability has six ideal wave patterns as basic solutions: oblique plane traveling zig and zag waves (stripes), rectangles traveling in the horizontal and vertical directions, oblique plane standing waves, standing rectangles, and alternating waves characterized by periodic reversals between zig and zag standing waves. In the pattern reported here, local patches of approximate right-traveling zag waves ($A_3 \neq 0, A_1, A_2, A_4 \approx 0$), right-traveling zig waves ($A_2 \neq 0, A_1, A_3, A_4 \approx 0$), right-traveling rectangles ($A_2 \approx A_3, A_1, A_4 \approx 0$), and small patches of standing rectangles or alternating waves ($|A_1| \approx |A_2| \approx |A_3| \approx |A_4|$) can be observed. To locate these patterns in space and time, we decompose the spatial domain into 32×16 cells and use local averages of the A_j in each cell and over 25 time steps. The presence of a particular wave type in a given cell and a given instant of time is determined by a threshold condition; e.g., for a zag wave we require $|A_j|/|A_3| < 0.1$ for $j = 1, 2, 4$.

The result of this calculation is visualized in Fig. 17. The horizontal axis in this figure comprises all 512 cell labels, with the labels in each of the 32 vertical bins concatenated and separated by vertical lines. The labels attached to the axis refer to the bin numbers. The cell labels from bottom to top in each bin are displayed left to right. If a cell at a given time satisfies the threshold criterion for a particular wave type, this is displayed green, blue, yellow, and red for zag waves, zig waves, TRs, and SRs or AWs, respectively.

A vertically integrated version of this figure is shown in Fig. 18. Here the size of the vertical region (number of cells) in each bin that is covered by a particular wave type is plotted versus bin number and time.

As expected we see mainly zag waves in these figures. Moreover, these waves are found in all regions with high
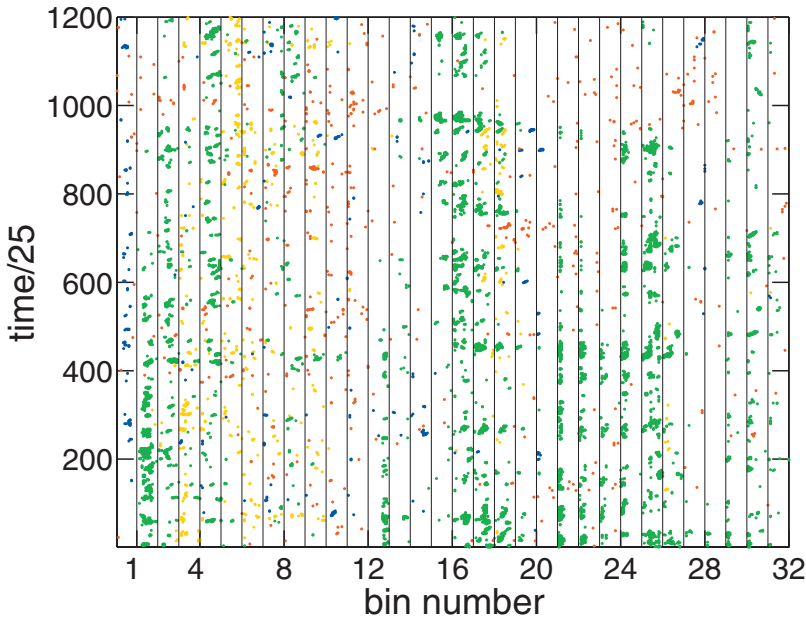
FIG. 17. (Color) Location of zag waves, zig waves, traveling rectangles (TRs), and standing rectangles (SRs) or alternating waves (AWs) in time and space, averaged over 25 time steps and cells of size 20×30 pixels. On the horizontal axis the 16 cell labels in each of the 32 vertical bins are concatenated, with bottom to top displayed left to right. The presence of a zag wave, zig wave, TR, and SR or AW is marked green, blue, yellow, and red, respectively.

intensity of A_3 except in region 3 [cf. Fig. 13(a)]. In contrast, only few zig waves occur and these are more randomly distributed. In addition we find in the left part of the domain relatively large, vertically organized regions with traveling rectangles. Thus high-intensity regions of A_2 lead to TR waves rather than zig waves. There are many small and short patches covered by SR or AW patterns; these occur mainly when A_2 and A_3 have low intensities. We conclude that the dominant patterns are zag waves and right-traveling rectangles. The wave patches cover about 2% of all space-time cells.

VI. CONCLUSIONS

We have reported and analyzed a complex spatiotemporal pattern that occurred in electroconvection in the nematic liquid crystal I52. The pattern was observed slightly above the onset of convection, which is a supercritical Hopf bifurcation leading to two (zig and zag) pairs of counterpropagating

FIG. 18. Number of cells, N, in each vertical bin showing (a) a zag wave, (b) a zig wave, (c) a TR, and (d) a SR or an AW as function of time ($t/25$) and bin number (l). Same axis labels for all four plots.

traveling rolls propagating in oblique directions relative to the director. Mathematically this kind of (oblique Hopf) instability is described by a system of four coupled Ginzburg-Landau equations [20–22], governing the evolution of slowly varying envelopes of four traveling plane-wave trains. In the present work, instead of simulating the Ginzburg-Landau system, we have extracted the envelopes from the experimental data using a demodulation analysis. In order to characterize the dynamics of the pattern, we have applied a variety of diagnostic tools to the envelopes, including the calculation of average intensities and spatial correlation lengths, global and local Karhunen-Loève decompositions in Fourier space and physical space, the location of holes in time and space, the identification of coherent vertical structures, and estimates of Lyapunov exponents. These methods are general and can be applied as well to other experimentally recorded or numerically computed complex space-time data.

One of the main characteristics of our pattern is the appearance of active and inactive regions extended in the vertical (parallel to the director) direction, resulting in significantly shorter correlation lengths in the horizontal than in the vertical direction. We have located the vertical coherence regions and coherent structures using a temporal correlation analysis, in which the boundaries between adjacent regions were identified through minimal nearest-neighbor correlations. The picture emerging from this analysis is that of a coupled spatial system, with strong coupling within the coherence regions and weak coupling between different regions. The effective number of degrees of freedom in each region was studied via Karhunen-Loève decompositions, showing that significantly fewer KLD modes contribute to the high-intensity envelopes A_2 and A_3 than to the low-intensity envelopes A_1 and A_4. It is tempting to assume that A_1 and A_4 are slaved by A_2 and A_3, but this can only be verified by investigating the Ginzburg-Landau system for the oblique Hopf instability in a parameter range showing the type of pattern recorded in this experiment.
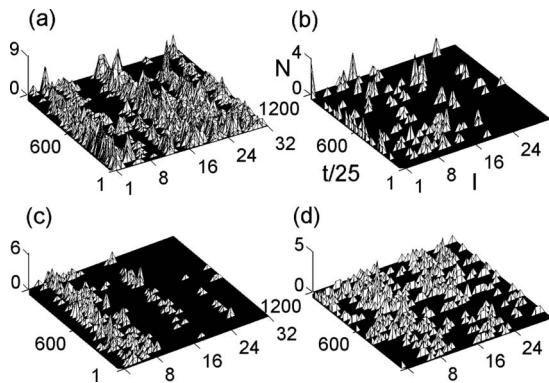
To diagnose the chaotic nature of the pattern, we have computed the KLD dimension $D_{KLD}(r)$ in spatial subsystems of increasing size. For sufficiently large r we found a perfect linear scaling of $D_{KLD}(r)$ with the subsystem size, indicating that the KLD dimension is an extensive quantity. Although there is no rigorous mathematical theory relating the KLD dimension to the Lyapunov or correlation dimension of a chaotic attractor, this scaling suggests that our pattern exhibits extensive spatiotemporal chaos. The chaoticity of the dynamics has also been confirmed by estimating the largest Lyapunov exponent from embedding calculations for a variety of time series, which resulted in positive exponents for all time series examined. We note that the embedding methods used to estimate the largest Lyapunov exponent only succeeded on the demodulated (slowly varying) data. Embedding calculations for the original, nondemodulated time series failed completely because of the fast oscillations present in them; only after demodulation was the time-series analysis feasible. This observation deserves further investigation.

Our pattern differs from the spatiotemporally chaotic pattern reported by Dennin *et al.* [9,11,15], which also was found in electroconvection in the nematic I52 slightly above the oblique Hopf instability, but for another set of material parameters and for a thicker cell (28 μm). The pattern of Dennin *et al.* [9,11,15], referred to as extended chaos type 1, is extended throughout the cell, whereas our pattern shows the active and inactive regions mentioned before. Moreover, in the pattern reported in [9,11,15], local patches of persisting alternating waves have been observed, which are characterized by an alternation between standing waves in the two oblique directions. The alternating waves require all four envelopes to have roughly equal amplitudes, which is not the case for our pattern. Instead, the analysis of ideal wave patterns performed in Sec. V F shows that zag-right waves and right-traveling rectangles are the favored patterns, and these patterns occur dominantly in the high-activity regions. In the low-activity regions the dynamics appears highly chaotic.

Whether the presence of the active and inactive regions is a form of spatiotemporal intermittency [57,58] is open at this point. Spatiotemporal intermittency is characterized by the coexistence of regions with regular or laminar behavior and regions with turbulent behavior. For our pattern, the active regions have smaller KLD dimensions and show a higher percentage of wave patches than the inactive regions. Thus it is tempting to identify the active regions with laminar regions, although the dynamics is still chaotic. To decide about spatiotemporal intermittency requires careful parameter studies regarding the widths of these regions. Preliminary experiments performed with the sample cell showed that the widths are very sensitive to variations in the conductivity. When $\sigma_\perp$ is increased, the widths of the inactive regions slightly above the onset become smaller and eventually these regions disappear. For $\sigma_\perp = 4.1 \times 10^{-8}$ Ω^{-1} m^{-1} a spatially uniform state is observed, similar to the state reported by Dennin *et al.* [9,11,15]. The inactive regions also get smaller when the voltage is increased beyond the onset value.

A mechanism or building block for the observed state has not yet been identified. Egolf *et al.* [59] claimed that spatially localized dislocation nucleation events are a main

mechanism underlying spiral defect chaos. Their claim is supported by theoretical studies of Rayleigh-Bénard convection in which these events are revealed in a temporally local first Lyapunov vector. In a later paper Jayaraman *et al.* [60] suggested that this claim does not generalize to domain chaos in that there is not a simple relation between defect dynamics and the largest Lyapunov exponent. Generally the existence of building blocks for spatiotemporal chaos remains to be difficult to establish, and is discussed somewhat controversial in the literature. Due to the lack of governing equations, computation such as those of Egolf *et al.* [59] and Tao *et al.* [60] could not be done for our experimental pattern. Calculations for the coupled Ginzburg-Landau equations describing the oblique Hopf instability should make it possible to perform a similar analysis, as well as to address questions such as for the scaling of the widths of the active and inactive regions when parameters are varied. The parameter regime for these equations that leads to the type of pattern reported here still has to be determined.

Nevertheless, there are some interesting similarities between the dynamics of the experimental pattern and of previous numerical studies of the Ginzburg-Landau equations utilized in our analysis of the weak electrolyte model. In the analysis of the experimental pattern we observe patches of A_2, A_3 reminiscent of regular solutions, destroyed by highly chaotic (even noisy) patches of A_1, A_4. A similar interplay between regular and chaotic patches was observed in the numerical zigzag spatiotemporal chaos described in [20]. Furthermore, the dynamics of the holes characteristic of the experimental pattern resembles the behavior of the holes observed in the extensive spatiotemporally chaotic pattern computed numerically in a weakly nonlinear analysis of the weak electrolyte model [19]. Both numerically computed STC patterns are bifurcating at the onset as does the experimental pattern analyzed here. Overall, the results of our analysis are consistent with the amplitude equations' description of the oblique Hopf instability, contributing in this way to a validation of the weak electrolyte model.

In this paper we have focused on a thorough analysis of a specific, particularly interesting pattern recorded for fixed material parameters of I52, and a fixed ac frequency and ac voltage slightly above the onset value. The main objective was to study the dynamics of the wave envelopes extracted from the pattern, in particular the diagnosis of extensive spatiotemporal chaos. Some of the other patterns found in the sample cell, for different values of the conductivity $\sigma_\perp$, such as worms, grid patterns, and alternating waves, are not described in this paper. Work toward determining the parameters of the standard model for these experiments is in progress. Together with estimates of the additional parameters occurring in the weak electrolyte model, this will enable us to compute the parameters in the Ginzburg-Landau system for the experiment reported here and related experiments, and to compare the simulated and recorded envelope dynamics.

In summary, the analysis presented in this paper shows that the study of slowly varying envelopes extracted from experimentally recorded space-time data is a useful approach to analyzing an observed spatiotemporal behavior above the onset of patterning. Combined with the methods of time se-

ries and pattern analysis utilized in this paper, this approach provides efficient tools for characterizing complex as well as ordered patterns, and to compare experiments with solutions of Ginzburg-Landau systems describing an instability. In particular, the ideal patterns predicted by the symmetries of the Ginzburg-Landau system, which are inherited from the instability, play the role of local building blocks from which more complicated patterns are formed. While for isotropic systems the description in terms of a finite set of plane-wave envelopes is problematic, anisotropic systems such as electrocon-

vection in nematic liquid crystals are ideally suited for this kind of analysis.

[1] M. C. Cross and P. C. Hohenberg, Rev. Mod. Phys. **65**, 851 (1993).

[2] I. S. Aranson and L. Kramer, Rev. Mod. Phys. **74**, 99 (2002).

[3] G. Ahlers, Physica A **249**, 18 (1998).

[4] S. M. Zoldi, J. Liu, K. M. S. Bejaj, H. S. Greenside, and G. Ahlers, Phys. Rev. E **58**, R6903 (1998).

[5] L. Kramer and W. Pesch, in *Macromolecular Systems: Microscopic Interactions and Macroscopic Properties*, edited by H. Hoffmann, M. Schwoerer, and T. Vogtmann (Wiley, New York, 2000), pp. 250–294.

[6] W. Pesch and U. Behn, in *Evolution of Spontaneous Structures in Dissipative Continuous Systems*, edited by F. H. Busse and S. Müller (Springer, New York, 1998), pp. 335–383.

[7] A. Buka, N. Éber, and W. Pesch, electronic-Liquid Crystal Communications, 2005/Jul/12 04:29:54 (2005), http://www.e-lc.org/docs/2005_07_12_04_29_54.

[8] R. Ribotta, A. Joets, and L. Lei, Phys. Rev. Lett. **56**, 1595 (1986).

[9] M. Dennin, Ph.D. thesis, Department of Physics, University of California–Santa Barbara, 1995 (unpublished).

[10] M. Dennin, G. Ahlers, and D. S. Cannell, Phys. Rev. Lett. **77**, 2475 (1996).

[11] M. Dennin, D. S. Cannell, and G. Ahlers, Phys. Rev. E **57**, 638 (1998).

[12] U. Bisang and G. Ahlers, Phys. Rev. E **60**, 3910 (1999).

[13] M. Treiber, N. Éber, A. Buka, and L. Kramer, J. Phys. II **7**, 649 (1997).

[14] M. Dennin, M. Treiber, L. Kramer, G. Ahlers, and D. S. Cannell, Phys. Rev. Lett. **76**, 319 (1996).

[15] M. Dennin, G. Ahlers, and D. S. Cannell, Science **272**, 388 (1996).

[16] M. Treiber and L. Kramer, Mol. Cryst. Liq. Cryst. **261**, 311 (1995).

[17] M. Treiber and L. Kramer, Phys. Rev. E **58**, 1973 (1998).

[18] G. Dangelmayr and I. Oprea, Mol. Cryst. Liq. Cryst **413**, 305 (2004).

[19] I. Oprea and G. Dangelmayr, Eur. J. Mech. B/Fluids **27**, 726 (2008).

[20] I. Oprea, I. Triandaf, G. Dangelmayr, and I. Schwartz, Chaos **17**, 023101 (2007).

[21] G. Dangelmayr and M. Wegelin, in *Pattern Formation in Continuous and Coupled Systems*, IMA Volumes in Mathematics and Its Applications 115, edited by M. Golubitsky, D. Luss, and S. Strogatz (Springer, New York, 1999), pp. 33–47.

[22] G. Dangelmayr and I. Oprea, J. Nonlinear Sci. **18**, 1 (2008).

[23] M. Silber, H. Riecke, and L. Kramer, Physica D **61**, 260 (1992).

[24] M. Wegelin, Ph.D. thesis, University of Tübingen, 1993 (unpublished).

[25] J. Grebovicz and B. Wunderlich, Mol. Cryst. Liq. Cryst. **76**, 287 (1981).

[26] I. Rehberg, B. L. Winkler, M. de la Torre Juárez, S. Rasenat, and W. Schöpf, Festkoerperprobleme/Advances in Solid State Physics **29**, 35 (1989).

[27] N. R. Badnell, Phys. Rev. A **42**, 209 (1990).

[28] J. Shi, C. Wang, V. Surendranath, K. Kang, and J. T. Gleeson, Liq. Cryst. **29**, 877 (2002).

[29] T. Pohl, U. Feudel, and W. Ebeling, Phys. Rev. E **65**, 046228 (2002).

[30] T. John and R. Stannarius, Phys. Rev. E **70**, 025202(R) (2004).

[31] H. Bohatsch and R. Stannarius, Phys. Rev. E **60**, 5591 (1999).

[32] T. John, R. Stannarius, and U. Behn, Phys. Rev. Lett. **83**, 749 (1999).

[33] S. Nasuno, O. Sasaki, S. Kai, and W. Zimmermann, Phys. Rev. A **46**, 4954 (1992).

[34] I. Rehberg, S. Rasenat, and V. Steinberg, Phys. Rev. Lett. **62**, 756 (1989).

[35] I. Rehberg, F. Horner, and G. Hartung, J. Stat. Phys. **64**, 1017 (1991).

[36] L. Kramer and W. Pesch, in *Pattern Formation in Liquid Crystals*, edited by A. Buka and L. Kramer (Springer, New York, 1995), pp. 221–256.

[37] U. Finkenzeller, T. Geelhaar, G. Weber, and L. Pohl, Liq. Cryst. **5**, 313 (1989).

[38] C. Kamaga and M. Dennin, Phys. Rev. E **65**, 057204 (2002).

[39] J. T. Gleeson, N. Gheorghiu, and E. Plaut, Eur. Phys. J. B **26**, 515 (2002).

[40] S. Rasenat, G. Hartung, B. L. Winkler, and I. Rehberg, Exp. Fluids **7**, 412 (1989).

[41] R. Vautard and M. Ghil, Physica D **35**, 395 (1989).

[42] S. Ciliberto and B. Nicolaenko, Europhys. Lett. **14**, 303 (1991).

[43] L. Sirovich and A. Deane, J. Fluid Mech. **222**, 251 (1991).

[44] J. Lega and S. Fauve, Physica D **102**, 234 (1997).

[45] J. Lega, Physica D **152-153**, 269 (2001).

[46] J. Lega, in *Dynamics and Bifurcation of Patters in Dissipative Systems*, World Scientific Series B, edited by G. Dangelmayr and I. Oprea (World Scientific, Singapore, 2004), Vol. 12, pp. 143–157.

[47] J. L. Kaplan and J. A. Yorke, in *Functional Differential Equa-*

tions and Approximation of Fixed Points, Springer Lecture Notes in Mathematics Vol. 730, edited by H.-O. Peitgen and H.-O. Walter (Springer, New York, 1979), pp. 228–237.

[48] J. P. Eckmann and D. Ruelle, Rev. Mod. Phys. **57**, 617 (1985).

[49] P. Grassberger, Phys. Scr. **40**, 346 (1989).

[50] A. Torcini, A. Politi, G. P. Puccioni, and G. D'Alessandro, Physica D **53**, 85 (1991).

[51] D. A. Egolf and H. S. Greenside, Nature (London) **369**, 129 (1994).

[52] R. Carretero-Gonzáles, S. Ørstavik, J. Huke, D. S. Broomhead, and J. Stark, Chaos **9**, 466 (1999).

[53] S. M. Zoldi and H. S. Greenside, Phys. Rev. Lett. **78**, 1687 (1997).

[54] A. Jayaraman, J. D. Scheel, H. S. Greenside, and P. F. Fischer, Phys. Rev. E **74**, 016209 (2006).

[55] M. Das, B. Chakrabarti, C. Dasgupta, S. Ramaswamy, and A. K. Sood, Phys. Rev. E **71**, 021707 (2005).

[56] P. Jung, J. Wang, R. Wackerbauer, and K. Showalter, Phys. Rev. E **61**, 2095 (2000).

[57] K. Kaneko, Prog. Theor. Phys. **74**, 1033 (1985).

[58] H. Chaté and P. Manneville, Physica D **32**, 409 (1988).

[59] D. A. Egolf, H. V. Melnikov, W. Pesch, and R. E. Ecke, Nature (London) **404**, 733 (2000).

[60] A. Jayaraman, J. D. Scheel, H. S. Greenside, and P. F. Fischer, Phys. Rev. E **74**, 016209 (2006).